Special Issue: *Australopithecus sediba*

The Shoulder, Arm, and Forearm of *Australopithecus sediba*

STEVEN E. CHURCHILL
Department of Evolutionary Anthropology, Duke University, Durham, NC 27708, USA; and, Evolutionary Studies Institute, University of the Witwatersrand, WITS 2050, Johannesburg, SOUTH AFRICA; churchy@duke.edu

DAVID J. GREEN
Department of Anatomy, Campbell University, P.O. Box 4280, Buies Creek, NC 27506, USA; Department of Anatomy, Midwestern University, 555 31st St., Downers Grove, IL 60515, USA; and, Evolutionary Studies Institute, University of the Witwatersrand, WITS 2050, Johannesburg, SOUTH AFRICA; dgreen@campbell.edu

ELEN M. FEUERRIEGEL
Primate Evolutionary Biomechanics Laboratory, Department of Anthropology, Box 353100, University of Washington, Seattle, WA 98195-3100, USA; and, Evolutionary Studies Institute, University of the Witwatersrand, WITS 2050, Johannesburg, SOUTH AFRICA; efeuer@uw.edu

MARISA E. MACIAS
Division of Anthropology, American Museum of Natural History, Central Park West at 79th Street, New York, NY 10024, USA; mmacias@amnh.org

SANDRA MATHEWS
Paul Scherrer Institut, Forschungsstrasse 111, 5232 Villigen PSI; and, Institute of Evolutionary Medicine, University of Zurich, Winterthurerstrasse 190, CH-8057 Zurich, SWITZERLAND; sandra.mathews@psi.ch

KRISTIAN J. CARLSON
Department of Integrative Anatomical Sciences, Keck School of Medicine, University of Southern California, Los Angeles, CA 90033, USA; and, Evolutionary Studies Institute, University of the Witwatersrand, WITS 2050, Johannesburg, SOUTH AFRICA; kristian.carlson@usc.edu

PETER SCHMID
Anthropological Institute and Museum, University of Zurich, Winterthurerstrasse 190, CH-8057, Zurich, SWITZERLAND; and, Evolutionary Studies Institute, University of the Witwatersrand, WITS 2050, Johannesburg, SOUTH AFRICA; peterschmid2014@gmail.com

LEE R. BERGER
Evolutionary Studies Institute, School of Geosciences, University of the Witwatersrand, WITS 2050, Johannesburg, SOUTH AFRICA; profleeberger@yahoo.com

submitted: 15 August 2017; accepted 10 December 2018

ABSTRACT

The bones of the pectoral girdle and upper limb are well represented among the fossils thus far recovered from Malapa (Gauteng Province, South Africa). Malapa Hominin 2, a partial skeleton representing an adult female of *Australopithecus sediba*, preserves a largely complete right pectoral girdle and upper limb, including the most complete scapula yet recovered of an adult australopith, as well as fragmentary remains from the left side. The subadult male holotype specimen of *Au. sediba*, Malapa Hominin 1, preserves portions of the right clavicle, right and left humeri, right ulna, and right radius. This wealth of remains reveals a shoulder, arm, and forearm in *Au. sediba* that was predominantly primitive in its morphology, and which suggests the retention of substantial climbing and suspensory ability.

This special issue is guest-edited by Scott A. Williams (Department of Anthropology, New York University) and Jeremy M. DeSilva (Department of Anthropology, Dartmouth College). This is article #4 of 9.

INTRODUCTION

The upper limbs are well represented in the Malapa hominins. The subadult male specimen Malapa Hominin 1 (MH1) preserves portions of the right clavicle, right and left humeri, right ulna, and right radius (as well as a third metacarpal, most likely from the right side [see Kivell

***P**aleo**A**nthropology* **2018: 234–281.**
doi:10.4207/PA.2018.ART114

ISSN 1545-0031

et al. 2018]). To date, remains of the MH1 scapulae have not been recovered, although a very small fragment (U.W. 88-113) may represent a portion of the root of the spine of one of MH1's scapulae (Berger et al. 2010). Since its identification as to element is currently uncertain, that specimen is not described here. MH2 preserves a largely complete right upper limb (clavicle, scapula, humerus, radius and ulna; MH2 also preserves 20 bones of the right hand, which are described in Kivell et al. [2018]). The left upper limb of MH2 is represented by fragments of the clavicle, scapula, and humerus (as well as six bones of the left hand [Kivell et al. 2018]). While these fossils vary in their degree of completeness—from the largely intact bones of the MH2 right upper limb to the relatively small fragments of the bones of her left upper limb—the surface condition of the bones is, with only a few exceptions, uniformly good (see Val et al. 2015), and morphological features such as muscle scars and joint surfaces are easily discerned. In addition to the morphology that is the focus of this description, the upper limb of MH2 also preserves evidence of perimortem trauma that may be related to the cause of death of this individual (L'Abbé et al. 2015), as well as evidence of pathological conditions that may bear upon the lifeways of *Australopithecus sediba* (Mathews 2017; Mathews et al. 2016). Here we provide detailed morphological descriptions of each element by individual, followed by brief discussion of upper limb morphology in *Au. sediba* relative to that of known hominin species in the genera *Australopithecus* and *Homo*. Three-dimensional surface scans of most of the specimens described here are available for free download on MorphoSource (www.morphosource.org).

CLAVICULAE

CLAVICLE OF MALAPA HOMININ 1 (MH1)

U.W. 88-1: Lateral Half Of Right Clavicle

Preservation. Roughly half of the right clavicle of MH1 is preserved in the 69.8mm long fragment U.W. 88-1 (Figure 1). An additional 22.8mm of the medial shaft is represented by a natural cast of the anterior surface of the bone preserved in the matrix block from which the specimen was recovered. The SI diameter of the natural cast is larger than that of the adjacent diaphysis of the fossil itself, indicating that the shaft was beginning to expand towards the sternal end in the area of the break. This suggests that the diaphysis broke roughly mid-way between the conoid tubercle and the sternal articular surface. The shaft is broken obliquely from anteromedial to posterolateral. Posteriorly, the edges of the break are weathered and matrix occludes the medullary cavity; the anterior margin, however, suffered the detachment of an approximately 2–3mm thick piece of cortical bone during preparation of the specimen (this small fragment remains embedded in the matrix block). There are several longitudinal cracks on the superior surface of the diaphysis, as well as multiple hairline fractures (primarily on the posterior diaphyseal surface). The posterior surface is discolored beginning ca. 12.5mm from the lateral end of the clavicle and continuing to the medial break. The surface of the lateral half of this area appears weathered and eroded (this surface was exposed on the outside of the block), while that of the medial half is covered by hairline fractures in an intersecting spiderweb pattern. Erosion to the posterior shaft affects the area of the angular margin and the conoid tubercle, making it difficult to assess the morphology of this region. The lateral part of the acromial extremity is badly weathered, exposing cancellous bone (which has matrix embedded in it) over the entire lateral insertion area of *M. trapezius* and possibly over the posterior portion of the acromial facet. The preserved portion of the acromial facet is irregular and appears to represent the metaphyseal surface of an unfused acromial epiphysis.

Figure 1. MH1 right clavicle U.W. 88-1 in superior, posterior, inferior, and anterior views (scale bar in cm).

Morphology. The clavicle, based on the curvatures observable in the lateral shaft, appears to have had a marked S-shape in the transverse plane (as do humans and chimpanzees [Voisin 2006]). Based on the position of the conoid tubercle relative to the lateral end of the acromial extremity and the midshaft region, the bone appears to have been slightly longer than that of MH2. Assuming the diaphyseal break occurs mid-way between the conoid tubercle and the sternal articular surface, an estimated conoid length (Churchill 1994) of 94.5mm can be obtained. Adding the mediolateral (ML) distance from the conoid tubercle to the acromial facet provides a rough estimate of maximum length of 116mm. The mid-proximal shaft (at the medial end of the fragment in the approximate vicinity of mid-conoid length) has an anteroposterior (AP) diameter of 10.9mm and a superoinferior (SI) diameter of 7.8mm, and the circumference is 31mm. At the approximate midshaft, the specimen has a maximum diameter (AP) of 10.4mm, a minimum diameter (SI) of 7.4mm and a circumference of 28mm. The cross-sectional outline at midshaft is ovoid (dorsoventrally elongated), and the inferior surface is flattened. Based on the angular relationship of the acromial extremity to the lateral portion of the shaft, the acromial end appears to have been inferiorly inflected to roughly the same extent as seen in MH2 (perhaps indicating a higher shoulder position than seen in humans [Ohman 1986]).

The *M. deltoideus* origin is weakly developed; the anterior surface of the lateral curve is rough to the touch and surface rugosity can be made out under magnification, but a clear muscle scar is not discernable without magnification. The subclavian sulcus is very shallow and poorly delimited. It is not possible to discern lines of attachment of *M. trapezius* even in the area in which surface damage from weathering is minimal or absent, although a low rounded ridge on the superior surface of the lateral shaft may mark the anteromedial line of the insertion of the muscle. The conoid tubercle projects dorsally as a posterior flange, without a distinct tubercle on the inferior surface (erosion to the dorsal surface of the shaft precludes evaluation of the dorsal aspect of the conoid tubercle). Shaft diameters at the conoid tubercle are 13.4mm AP by 7.6mm SI (including the tubercle). Although the area is affected by weathering, there appears to have been an angular margin separating inferior from posterior surfaces, as has been noted in *Au. afarensis* specimens A.L. 288-1 (Johanson et al. 1982), A.L. 333x-6/9 (Lovejoy et al. 1982) and A.L. 438-1 (Drapeau et al. 2005). As with A.L. 333x-6/9, the shaft has a rhomboidal cross-sectional outline in this area. Above the conoid tubercle the diaphysis has a smooth, rounded transition to the superior surface, as has been observed in chimpanzees as well as one specimen attributed to *Au. africanus,* StW 606 (Partridge et al. 2003), but unlike other *Au. africanus* specimens StW 431 and StW 582 (which have the human-like condition [SEC personal observation]). This differs from the typical human morphology of a relatively flat superior surface, with a distinct edge between the superior and posterior surface. The trapezoid line appears as a low, poorly developed ridge extending to the lateral extent of the acromial extremity.

The acromial extremity is anteroposteriorly expanded as in humans (and unlike apes [Swindler and Wood 1973]), and the preserved portion has a maximum AP dimension of 17.3mm and a maximum SI dimension of 9.3mm. The preserved portion of the articular surface for the acromion process is a rough and irregular oval (perhaps representing an unfused metaphyseal surface), measuring 7.1mm AM-PL by 5.2mm SI. It is not possible to determine how much of the articular surface might be missing from erosion.

CLAVICLE OF MALAPA HOMININ 2 (MH2)

U.W. 88-38 & -142: Complete Right Clavicle

Preservation. The right clavicle of MH2 is represented by two conjoining fragments—an approximately 64.5mm long lateral portion (U.W. 88-38) and an approximately 46.5mm long medial portion (U.W. 88-142) (Figure 2). The broken edges do not refit cleanly, but continuity in the contours of the anterior and inferior surfaces across the break suggest that not more than a millimeter or so of the shaft length has been lost. The broken margin of the shaft of the lateral fragment is slightly angled from superolateral to inferomedial. The edges of the break are not rounded by taphonomic processes, but present sharp edges where not occluded by matrix. The conjoining surface of the medial fragment is more irregular; its anterior portion is slightly angled from superolateral to inferomedial (that is, forming the mirror-image of the conjoining surface), while the posterior portion is missing a triangular fragment with a height of 6.5mm and a base of 6mm and with an angled surface oriented anterolaterally to posteromedially. The broken margins of the medial fragment are more rounded and appear abraded. The endosteal space of both fragments is occluded with matrix. The conjoining surface is limited to the anterior inferior part of the diaphysis, and a crack that varies 1–2mm in width separates the external cortical surfaces of the anterior and superior diaphysis. With the exception of this small amount of cortical bone lost from the broken margins and the missing triangular fragment on the posterior surface of the diaphysis, the bone is complete.

The surface preservation of the lateral fragment is better than that of the medial piece. The medial fragment appears to be less heavily mineralized, and accordingly during preparation from the matrix it experienced exfoliation of a thin layer of the subperiosteal surface over much of the specimen. This slight surface damage appears to have obscured some of the ligamentous markings in the area of the costal tuberosity. Rugosity along the line of attachment of the superior margin of *M. pectoralis major* can still, however, be clearly observed. Despite some surface damage, the gross morphology of the medial clavicle remains intact, and the slight irregularities in surface bone do not impede morphological interpretation. Surface detail is much better preserved in the lateral fragment. A small (ca. 2mm by 1mm) fragment of cortical bone has been displaced from the anterior border of the acromion process, and is suspended in adherent matrix. This appears to be the only evidence of taphonomic damage to the lateral fragment of the clavicle.

Morphology. The conjoined fragments provide an estimated maximum length (M-1: here and through-out the text, M-# refers to measurement numbers in Martin [1928])

Figure 2. MH2 right (U.W. 88-38 & -142) and left (U.W. 88-94) clavicles in superior, anterior, inferior, and posterior views (scale bar in cm).

of 107.5mm and an estimated articular length (Trinkaus 1983) of 99mm. At midshaft the specimen has a maximum diameter of 9.5mm, a minimum diameter of 6.5mm and a circumference of 26mm. The specimen has an estimated conoid length (from the middle of the sternal articular surface to the middle of the conoid tubercle [Churchill 1994]) of 86.6mm. The diaphyseal break occurs exactly at the middle of the conoid length. The mid-proximal shaft diameters are 7mm SI and 9.3 AP, and the mid-proximal circumference is 26mm. The clavicle overall has an S-shaped curvature in the transverse plane, as in humans and chimpanzees (Voisin 2006).

The sternal articular surface forms an irregular trapezoid, wider anteroinferiorly than posterosuperiorly. The long axis of the joint is oriented anteroinferior-to-posterosuperior and is 16.2mm in AP diameter. The joint surface has its greatest diameter (15.9mm AS-PI) anteriorly and narrows posteriorly (measuring 9.3mm AS-PI at its posterior extent). The anterior third of the joint surface is entirely occupied by an oval defect (14.5mm AS-PI by 7.7mm AI-PS). The surface of the defect is irregular and pitted and attains a depth of ca. 4mm in places, and is bordered inferiorly and anteriorly by a raised margin of bone (which attains a maximum thickness of ca. 3mm). The defect appears superficially like metaphyseal surface, and it is possible that the sternal epiphysis was only partially fused. However, the margin of the unaffected, adjacent joint surface does not appear broken (as it would if the unfused portion of the epiphysis had broken away). Additionally, the raised and thickened margin of the external edges of the defect is more pronounced, rugose and irregular than the normally thin and clearly defined line of attachment of the joint capsule normally seen in this area. The defect may represent osteoarthritic degeneration (the thickened margin representing marginal lipping and the irregular surface representing porosity [see Mathews 2017]). Among modern humans the joint surface often extends anteroinferiorly onto the diaphysis, producing an articular corner which articulates with the first costal cartilage. The sternal surface of the MH2 clavicle appears to have been similarly deflected, although the presence of the defect may be accentuating the appearance of the angle formed by the two parts of the joint surface.

The costoclavicular (rhomboid) ligament attachment appears as a shallow and indistinctly defined depression, largely devoid of surface morphology, on the inferior surface of the medial shaft. The depression is bounded anteriorly by a moderately developed and mildly rugose ridge extending some 30mm lateral of the joint margin. A similar ridge extends ca. 23mm from the articular margin along the anterosuperior corner of the medial shaft. These two ridges define the edges of the clavicular origin of *M. pectoralis major*. There is a very slight rugosity on the anteromedial and medial edges of the superior surface, which likely denote the anterior and medial margins of the *M. sternocleidomastoideus* origin, respectively. The medial shaft is triangular in cross section, with the base anterior and the apex posterior. Moving laterally, the shaft cross-sectional outline becomes more ovoid (dorsoventrally elongated) until it begins to flare in the area of the *M. deltoideus* for the acromial process.

The *M. deltoideus* origin is weakly developed, being palpable but with minor rugosity on the anterior margin of the bone, and with the exception of a small tubercle and ridge laterally (adjacent to the acromial articular facet), it is seemingly absent on the inferior surface. The deltoid scar is positioned on the anterior surface of the lateral curve of the shaft, not on the superoanterior surface as in chimpanzees (in the Sterkfontein specimens StW 431 and StW 582 the deltoid scar is anteriorly and inferiorly positioned. In StW 431 there is a distinct facet present on the medial side of the muscle scar, and a moderately sharp crest separates the muscle attachment area from the superior surface of the shaft. There is also a crest separating the deltoid origin area from the insertion of *M. subclavius*. In StW 582 there is a small patch of rugosity in the same position as the facet in StW 431. Otherwise, the attachment is not visible). The subclavian sulcus is very shallow and poorly delimited, being somewhat more distinct laterally (just medial of the conoid tubercle) and harder to discern medially. The *M. trapezius* insertion presents as a distinct but nonrugose ridge on the superoposterior border, but without a distinct line of attachment on the posterior surface. The conoid tubercle is prominent in the form of a posterior flange. Shaft diameters at the conoid tubercle are 12.8mm AP by 7.8mm SI (including the tubercle). Continuous with the tubercle medially is a pronounced angular margin separating the inferior from the posterior surfaces, as has been reported in A.L. 288-1 (Johanson et al. 1982), A.L. 333x-6/9 (Lovejoy et al. 1982) and A.L. 438-1 (Drapeau et al. 2005). Similar, but perhaps less developed, angular margins can be seen in StW 431 and StW 582 (SEC personal observation). As with A.L. 333x-6/9, the shaft has a rhomboidal cross-sectional outline in this area. Above the conoid tubercle the diaphysis has a smooth, rounded transition to the superior surface, as has been observed in chimpanzees as well as StW 606 (Partridge et al. 2003), but unlike StW 431 and StW 582, which have the human-like condition of a relatively flat superior surface with a distinct edge between the superior and posterior surface (SEC personal observation). The trapezoid line is prominent and sharp. It extends anterolaterally for 5mm, and then flattens into a rounded and rugose line more similar to the condition seen in recent humans.

In anterior view and with the shaft held in the horizontal plane, the anterior acromial extremity can be seen to be mildly inferiorly-inflected (possibly indicating a higher shoulder position than seen in humans [Ohman 1986]). The acromial extremity is anteroposteriorly expanded as in humans (and unlike apes [Swindler and Wood 1973]), and has a maximum AP dimension of 19mm and a maximum SI dimension of 11.4mm. The scapular acromial articular surface is a large (13.3mm AM-PL by 10mm SI) oval, with a blunt but prominent lateral edge to the articular surface. The superior margin of the facet is sharp and projecting anteriorly, almost forming a roof over the superior part of the articular surface. Posteriorly the superior margin widens into a roughened, projecting tubercle continuous with the *M. trapezius* insertion area. The articular surface slopes moderately from superoanterior to inferoposterior. The lateral insertion area for *M. trapezius* (posterior to the articular facet) exhibits a smooth triangular surface approximately 9.8mm wide (SI) at its base and 12mm (AP) high. The inferior margin of the *M. trapezius* insertion area forms a distinct crest separating the muscle scar from the inferior surface, culminating at its inferoanterior corner as a pronounced tubercle. Continuing medially from the tubercle is a thick inferior margin of the acromial articular surface. These pronounced inferior borders, along with the trapezoid line medially, circumscribe a moderately deep fossa on the inferior surface of the acromial extremity.

U.W. 88-94: Acromial Extremity Of Left Clavicle

Preservation. U.W. 88-94 is a lateral left clavicle, broken medial of the conoid tubercle (see Figure 2). The maximum length of the preserved portion is 38.8mm, which includes the conoid tubercle and much of the angular margin medial to it. The shaft is broken at a steep angle, slanting from superolateral to inferomedial (thus the inferior surface extends ca. 9mm further medially than does the superior surface). The edges are not rounded by taphonomic processes, and are rather sharp where not obscured by matrix. The endosteal space is occluded with matrix. The condition of the bone is quite good and surface detail can be readily discerned.

Morphology. In most respects the morphology of the left lateral clavicle is similar to that of the right. The conoid tubercle is more prominent than on the right side. Viewed from inferior, the conoid tubercle appears as a featureless flange projecting posteriorly; in dorsal aspect a distinct tubercle with a rugose surface is visible. Shaft diameters at the conoid tubercle are 14.9mm AP by 7.6mm SI (including the tubercle). The angular margin is even more distinct in the left side, and again the shaft is rhomboidal in cross-sectional outline in the area of the angular margin. As in the right-side clavicle, the surface above the conoid tubercle has a smooth, rounded transition to the superior surface without a distinct edge between the superior and posterior surfaces.

As in the right, the trapezoid line appears as a distinct, prominent crest running towards the inferomedial corner of the acromial facet. A moderately-deep sulcus medial of the trapezoid line demarks the lateral extent of *M. subclavius.* The *M. deltoideus* origin is more pronounced on the left side, appearing as a rugose furrow 3.3mm wide (SI) extending ca. 9mm laterally from the broken margin on the anterior side of the shaft. Small tubercles adjacent to the anteromedial margin of the acromial facet demarcate the lateral-most extent of the muscle origin. Lines of attachment of *M. trapezius* on the lateral shaft are not distinct. On the acromial extremity the lateral insertion area for *M. trapezius* appears as a slightly roughened triangular surface approximately 11.5mm wide (SI) at its base and 13.1mm (AP) high. Again, as with the right-side bone, the prominent inferior margin of the muscle scar, in conjunction with the pronounced inferior margin of the acromial facet anteriorly and the trapezoid line medially, bounds a moderately-deep fossa on the inferior surface.

The acromial extremity is not as large in the left clavicle—the maximum AP dimension is 16.8mm and the maximum SI dimension is 11.1mm. The superior surface of the acromial extremity forms a shallow depression with a roughened surface (and with ML-oriented striations visible under magnification). The scapular acromial articular surface is a large (13.7mm AM-PL by 9.8mm SI) oval, with a blunt but prominent lateral edge to the articular surface. As with the right-side bone, the superior margin of the facet is sharp and projecting anteriorly, almost forming a roof over the superior part of the articular surface, and the articular surface slopes moderately from superoanterior to inferoposterior.

SCAPULAE

SCAPULA OF MALAPA HOMININ 2 (MH2)

U.W. 88-28 & -56: Partial Right Scapula

Preservation. These two specimens conjoin to form a nearly complete right scapula, lacking only the acromion, the tip of the coracoid process, and a small amount of the body medial of the glenoid fossa (Figure 3). The scapula is broken into superior (U.W. 88-56) and inferior (U.W. 88-28) portions by a fracture through the glenoid fossa and the body at the level of the root of the scapular spine. The superior portion preserves the upper half of the glenoid fossa and scapular neck, the scapular notch and superior angle, the root of the coracoid and the lateral spine medial of the acromion process. The fragment has a maximum length (ML from glenoid fossa to the vertebral border ca. 23mm superior to the medial root of the spine) of 71.5mm, and a maximum SI diameter of 24.3mm (from the superior angle to the break in the blade). The supraspinous fossa is occluded with matrix (further preparation of the specimen risks damaging the paper thin bone of the scapular body). The coracoid process is broken and the lateral portion of the *M. pectoralis minor* insertion and the origin of the long head of *M. biceps brachii* are missing. The break is triangular in cross section (with the apex at the superoposterior corner and the base running IL-PM). The superior fragment preserves only the lateral part of the base of the spine, which is in two pieces. The inferior fragment of the root is connected to the scapular neck in anatomical position, whereas a smaller (18.9mm ML by 11.2mm AP) superior fragment is ventrally displaced from the rest of the spine by approximately 2.5mm, and is suspended in adherent matrix. The acromion process is missing. Although several hairline fractures can be detected, the surface preservation is generally good and morphological features can be readily discerned.

The inferior fragment comprises the rest of the glenoid fossa and blade, as well as the medial root of the spine. This fragment measures ca. 102mm SI from the inferior angle to the middle of the broken surface superiorly. An S-shaped crack traverses the inferior portion of the fragment (starting laterally just above the *M. teres major* origin and ending medially roughly 20mm inferior to the intersection of the spine and vertebral border), and although the two parts of the fragment are still conjoined by matrix, the inferior portion has been very slightly displaced dorsally relative to the superior portion. The fracture does not appear to have propagated completely across the axillary border, such that the displacement of the inferior portion also appears to involve a very slight amount of plastic deformation of the axillary border roughly 70mm inferior of the glenoid margin. A second, somewhat smaller fracture parallels the first variably 25–10mm above it, but does not reach the lateral edge of the bone. Matrix adheres to most of the dorsal surface of the inferior fragment (further preparation is precluded by the fragility of the scapular body) and effectively obscures the dorsal surface. The manubrium (U.W. 88-172) and right first rib (U.W. 88-198) of MH2 remain attached to the dorsal scapula by matrix (these elements are described in Williams et al. [2018]). The vertebral border has been largely cleared of matrix (although a portion of it is obscured by the manubrium), and a roughly 300mm^2 triangular patch of matrix has been removed from the dorsal surface adjacent to the inferior portion of the vertebral border. The lateral root of the scapular spine (at the vertebral border) has also been cleared of matrix, but roughly 25mm of the spine lies buried in matrix before re-emerging for ca. 21mm before terminating in a break. Only the ventral part of the axillary border is exposed, as matrix obscures everything dorsal of the median axillary crest (crista medioaxillaris [Vallois 1932]). The infraglenoid tubercle and the inferior half of the glenoid fossa can be viewed in their entirety. Despite the existence of hairline fractures and small patches of abrasion, the surface preservation of the specimen is generally good and anatomical details not obscured by adherent matrix can be discerned without difficulty.

The two portions of the right scapula (U.W. 88-28 & -56) conjoin only at the glenoid fossa and scapular neck and at the vertebral border. Between these medial and lateral contact points a fissure up to 5mm wide separates the two opposing edges. The contacting edges of the glenoid fossa refit cleanly, however a small triangular piece of the joint surface is missing at the ventral margin (the missing piece has a height of 5mm and a base of 4.5mm).

To quantify the angular relationships between the glenoid fossa, spine, body, and vertebral and axillary borders,

Figure 3. MH2 scapular remains. Right scapula: U.W. 88-56 in anterior, superior, and posterior views; U.W. 88-28 in anterior view. Left scapula: U.W. 88-103 in anterior, superior, and posterior views; U.W. 88-104 in anterior, lateral, and posterior views; U.W. 88-197 in posterior and anterior views (scale bar in cm).

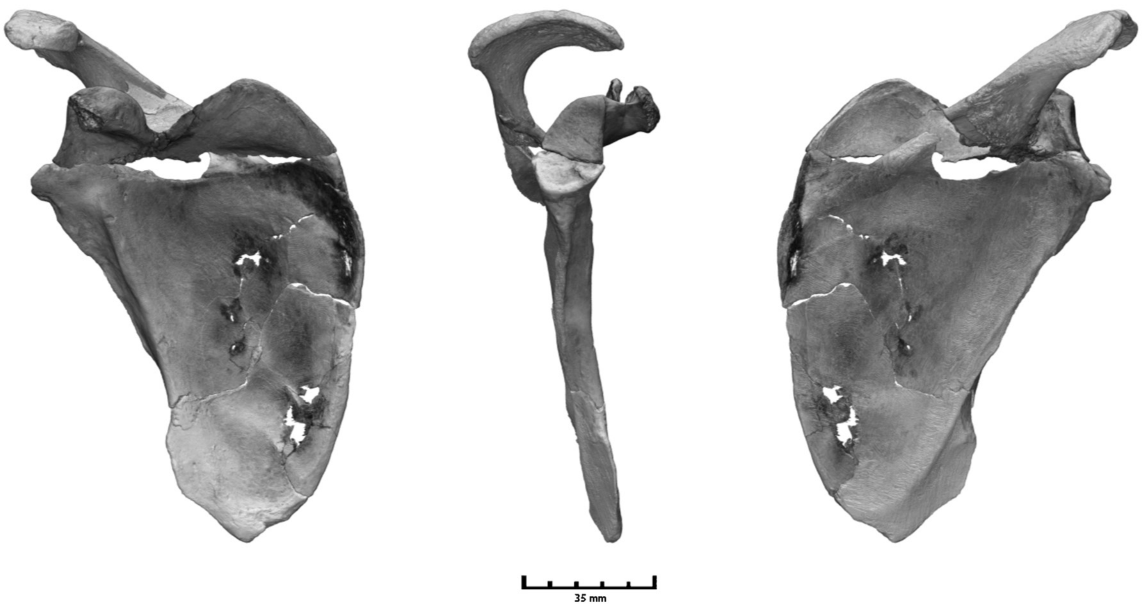

Figure 4. Digital rendering of the reconstructed MH2 right scapula in ventral, lateral, and dorsal views. In silico reconstruction involved segmenting individual renderings from high resolution image data, followed by rejoining the superior fragment (preserving much of the supraspinous fossa, the lateral root of the acromion, and the superior half of the glenoid fossa) with the body inferiorly. When possible, aligning separate fragments was performed at the level of individual trabecular struts crossing a break. The right scapula lacks the acromion process; thus, the left side acromion process was mirrored and aligned to obtain the best fit with overlapping preserved portions of the lateral spine.

as well as to measure some of the dimensions of the body, high resolution image data were acquired from the two portions of the MH2 scapula, matrix was digitally removed, and the two portions were virtually refit to reconstruct the scapula (for details, see Churchill et al. [2013]). The left side acromion process (U.W. 88-103) was also scanned, after which it was mirror-imaged and integrated into the right side reconstruction (Figure 4).

Morphology. The scapula has an anatomical breadth (M-1) of 124.3mm and an anatomical length (M-2) of 83.4mm. The supraspinous fossa breadth (following Alemseged et al. [2006]) measures 57.4mm, while the infraspinous fossa breadth (again following Alemseged et al. [2006]) is 86.7mm. The scapula is ape-like in having a cranially-oriented glenoid fossa, as reflected in its low glenoaxillary angle (132.6°: angle taken following Haile-Selassie et al. [2010]; 123.4° following Churchill et al. [2013]) and low bar-glenoid angle (131.2°: angle taken following Stern and Susman [1983]). The bar-glenoid angle of MH2 is intermediate between those of specimens of *Au. afarensis* (A.L. 288-1: 132.2°; KSD-VP-1/1: 134°; Green and Alemseged [2012]) and *Au. africanus* (Sts 7: 128°; StW 162: 124.3°; Green and Alemseged [2012]). Also, as in African apes, the specimen has a markedly cranially-directed spine (spinomedial angle=57.9°: angle taken following Alemseged et al. [2006]), and a relatively large attachment area for *M. supraspinatus.* The relative proportions of the supraspinous and infraspinous fossae are very similar to those of the juvenile *Au. afarensis* specimen DIK-1-1 (Alemseged et al. [2006]), and with a supraspinous/infraspinous breadth ratio intermediate between those of *Homo* and the African apes (see below). The axillary and vertebral borders meet at an acute angle (axillary-vertebral angle=31.8°: angle taken following Haile-Selassie et al. 2010]).

The glenoid fossa has a maximum length (M-12) of 30.9mm and a maximum breadth (M-13) of 19.5mm. The articular length and breadth of the glenoid fossa (Churchill and Trinkaus 1990) are 26.4mm and 14.7mm, respectively. The glenoid fossa of MH2 is thus narrow relative to its length when compared to modern humans. The specimen lacks a distinct glenoid notch on the ventral aspect of the glenoid fossa; instead the ventral margin tapers gently posteriorly as it approaches the top of the fossa, giving the articular surface more of a tear-drop than a piriform shape. The fossa is moderately deep.

The supraglenoid tubercle is low and rounded and smooth over most of its surface, but with some minor rugosity towards the root of the coracoid process. The neck of the coracoid process is relatively thin, and projects anteriorly at almost a right angle to the long axis of the glenoid fossa. The lateral margin of the neck of the coracoid forms a sharp crest, running from the supraglenoid tubercle posteriorly to the posterior surface of the coracoid process anteriorly. The coracoid process presents a smooth attachment area for the conoid and trapezoid ligaments. A small crest on the anterior surface of the coracoid likely represents the medial part of the *M. pectoralis major* insertion. The scapular notch is deep and U-shaped. The vertebral border adjacent to the superior angle is thickened, and a small sulcus running ca. 4mm lateral of the vertebral border marks the superior insertion point of *M. serratus anterior*. On the dorsal aspect of the scapular neck, the lateral root of the spine projects dorsally at an approximately 85° angle to the long axis of the glenoid fossa; the lateral-most point on the root of the spine lies 13.6mm medial of the dorsal rim of the glenoid fossa at the same level. The thickness (SI) of the lateral root of the spine cannot be determined due to damage in this area.

The infraglenoid tubercle presents as a large, rugose, and strongly projecting triangular feature. The tubercle extends 23.2mm below the inferior margin of the glenoid fossa, and is ca. 10mm wide (AP) at the point of its greatest development (just inferior of the glenoid fossa). The tubercle ends distally in a sharp and projecting median crest that runs distally approximately 29mm before disappearing dorsally into the adherent matrix. The median crest can be seen on the digital rendering to continue to course dorsally until it forms a thin, projecting dorsal bar along the medial margin of the *M. teres major* origin. This bar becomes distinct at the mid-point of the axillary border and continues inferiorly before ending about 10mm proximal to the inferior angle. The ventral margin of the axillary border is defined by a prominent ventral pillar (ventral bar), beginning proximally at the level of the mid-infraglenoid tubercle and extending distally down to the superior margin of the *M. teres major* origin, at which point it continues distally to the inferior angle as an ill-defined and less projecting pillar. The ventral bar and the infraglenoid tubercle/median crest form a deep ventral sulcus on the proximal third of the axillary border, which flattens and twists dorsally as it proceeds distally, such that the flattened sulcus occupies the dorsal side of the axillary border in its lower reaches. Adherent matrix obscures the dorsal surface, but on the digital rendering the sulcus can be seen to twist from the ventral to the dorsal side of the axillary border from proximal to distal. A small but distinct *M. teres major* flange projects laterally about 10mm from the distal continuation of the ventral bar. With two exceptions the morphology of the MH2 axillary border is very similar to that of StW 431 (however, in StW 431 the infraglenoid tubercle is not as pronounced and the ventral bar ends at the top of the flange for *M. teres major*).

The vertebral border is moderately thick. Two rugose oblique ridges (marking the intramuscular tendons of *M. subscapularis*) intersect the vertebral border on the ventral surface of the inferior body. The inferior position of these oblique ridges suggests that the inferior insertion area of *M. serratus anterior* was confined to the distal 7mm or so of the ventral body.

U.W. 88-103: Left Scapular Acromion Process

Preservation. This specimen is the complete acromion process of a left scapula, broken somewhere near the lateral root of the scapular spine (see Figure 3). The fragment has a maximum length (obliquely from the anterolateral corner of the acromion to the broken surface of the spine) of 55.5mm. The inferior portion of the break through the spine is curved both mediolaterally and ventrodorsally, and the broken surface is triangular in shape. The edges of the break are abraded in this region, and there is a small amount of matrix infilling of the broken spine (indicating breakage in antiquity). The superior part of the break forms a straight line in the sagittal plane, and is also abraded. Small (generally <1mm in diameter) patches of subperiosteal bone have been exfoliated in places, but overall the surface preservation is excellent and morphology of the specimen can be readily discerned.

Morphology. The acromion process forms a long narrow rectangle, with a maximum AP breadth (M-9) of 40.8mm and a maximum ML width of 19.1mm. The process has an SI thickness of 5.3mm at its center. The acromion is markedly curved in the sagittal plane (concave inferior surface and convex superior surface), as with African apes (SEC personal observation). Unlike African apes, however, the posterolateral corner is easily distinguished like that of most anatomically modern humans.

The origin area for *M. deltoideus* is relatively rugose along its entire length, and especially so along the anterior half of the lateral margin of the acromion. A distinct but low crest delimiting the line of insertion of *M. trapezius* can be made out on the superior surface, arising from the spinous portion of the fragment and arching anterolaterally until terminating in a rugose patch just lateral to the clavicular facet. The muscle attachment area medial to this line is smooth. Along the anteromedial margin, the superior and inferior surfaces are separated by a sharp crest, which extends proximally onto the spinous part of the fragment.

The articular surface for the clavicle is not positioned on the anteromedial corner of the acromion as it is in modern humans, but is situated on the medial border near the anterior end of the process. The facet thus faces medially, and is an irregular ovoid (with a slightly greater SI diameter dorsally than ventrally) measuring 12mm AP by 7.7mm SI. The articular surface is mildly convex SI and flat AP.

U.W. 88-104: Left Scapular Glenoid And Coracoid

Preservation. U.W. 88-104 is a left side scapular fragment, with a maximum length of 35.7mm, preserving the superodorsal portion of the glenoid fossa and the medial part of the coracoid process (see Figure 3). The coracoid process preserves only the medial 18.3mm, including the attachment surface for the conoid and trapezoid ligaments and the medial part of the *M. pectoralis major* insertion. The ventral side of the fragment exhibits primarily exposed trabecular bone intercalated with matrix. A 5.3mm by 4mm piece of matrix adheres to the inferodorsal surface of the glenoid fossa. Small surface cracks appear around the inferior part of the preserved glenoid fossa, and the surface of the entire fragment is white in color and abraded, having the appearance of being weathered. The surface is missing small patches of subperiosteal bone here and there, which were possibly removed during preparation.

Morphology. The glenoid fossa is not sufficiently preserved for measurement. Its dorsal margin is blunt and rounded, and its curvature appears similar to that of the right side glenoid fossa. Preserved morphology is in most respects similar to that of the right side scapula. The supraglenoid tubercle is not prominent, nor is it rugose. The neck of the coracoid process is relatively thin, but unlike its antimere, it projects anterosuperiorly at about 45º to the long axis of the glenoid fossa. The lateral margin of the neck of the coracoid forms a sharp crest, running from the supraglenoid tubercle posteriorly to the posterior surface of the coracoid process anteriorly. Abrasion to the anterosuperior surface of the coracoid process precludes evaluation of attachment areas for the conoid and trapezoid ligaments and *M. pectoralis major*.

U.W. 88-197: Fragment Of Left Scapular Body And Axillary Border

Preservation. This is a ca. 52mm (SI) by 34mm (ML) quadrilateral fragment of the lateral body of a left side scapula (see Figure 3). The fragment preserves the superior 10.5mm of the *M. teres major* flange and 43.7mm of the axillary border superior to the flange. Superiorly the axillary border is broken obliquely (from superomedial to inferolateral, and from superodorsal to inferoventral), while inferiorly the break lies roughly in the transverse plane. The surface of the body is cracked and abraded in places. A curved crack runs transversely across the inferior portion of the preserved body, and is visible on both the ventral and dorsal surfaces. Towards the medial end of this crack small detachments of bone result in a small hole (rough 3mm long by 0.5mm high) through the body.

Morphology. In every aspect, the observable morphology appears to be the exact antimere of MH2's right side scapula (U.W. 88-28). As in U.W. 88-28, a pronounced median crest can be seen on the dorsal edge of the axillary border on the superior part of the fragment, continuing distally to form a thin, projecting dorsal bar along the medial margin of the *M. teres major* origin. Also, as in U.W. 88-28, a prominent ventral bar runs inferiorly to the superior margin of the *M. teres major* origin, forming a flattened sulcus between it and the median crest on the upper half of the fragment. Again, as in U.W. 88-28, the sulcus twists dorsally as it moves distally, such that it comes to occupy the dorsal side of the axillary border on the inferior half of the fragment. This specimen also appears to have had a projecting *M. teres major* flange.

HUMERI

HUMERUS OF MALAPA HOMININ 1 (MH1)

U.W. 88-34, -42 & -88: Right Humerus Lacking Proximal Epiphysis

Preservation. The right humerus of MH1 is preserved in three fragments—the proximal end (U.W. 88-34), including the metaphyseal surfaces of the epiphysis of the head and the apophyses of the greater and lesser tubercles, and the bicipital groove; the shaft (U.W. 88-42) down to the level of the superior olecranon fossa; and, the distal end (U.W. 88-88), including the trochlea, capitulum, most of the olecranon fossa, and the metaphyseal surface for the unfused apophysis of the medial epicondyle (Figure 5). Corresponding edges of the proximal piece and the shaft can be seen to be congruous, and would likely conjoin cleanly were not matrix in the endosteal cavity of the shaft preventing refitting of the two pieces. Edges of the distal shaft and distal articular piece conjoin cleanly in the area of the radial fossa (but do not contact one another medially and laterally of this area).

The proximal fragment (U.W. 88-34) has a maximum length of 46.8mm, from the most proximal point on the unfused metaphysis to the most distally projecting point of the diaphysis. The proximal epiphysis is unfused and missing; the articular surface of the humeral head and both tubercles are absent (at a developmental age corresponding to a modern human of 12–13 [Berger et al. 2010]); it is likely that these three secondary growth centers would have been fused into a single epiphysis [Williams and Warwick 1980]). A portion of the posteromedial metaphyseal surface (underlying the humeral head portion of the epiphysis) is planed off from superolateral to anteromedial, leaving a triangular area of exposed cancellous bone 20.6mm wide at the base (superoanterior to inferoposterior) and 14.6mm high (superoposterior to inferoanterior). Immediately anterior to this area of damage, the anteromedial corner of the metaphysis (underlying the medial side of the lesser tubercle) has also been planed off or abraded over an area 15.7mm long (SP-IA) by 5.8mm wide (SA-IP), exposing trabecular bone. Exposed trabeculae in both of these areas are intercalated with matrix. Beyond these missing portions, the metaphyseal surface appears to have suffered no postmortem damage. A hairline crack encircles the proximal fragment below the surgical neck, but well above its distal break. Otherwise the surface is free of defects and morphological detail is well preserved.

The proximal fragment and diaphyseal fragment are separated by a transverse fracture in the area of the surgical neck. The distal fracture of the proximal piece is jagged, resulting in the fragment being longer dorsally than anteriorly. The proximal fracture of the diaphyseal fragment mirrors the conjoining surface of the proximal piece. Edges of the opposing broken surfaces on both fragments are sharp-to-moderately rounded under magnification, with matrix adhering to them and occluding the medullary space. At the anterior edge of the proximal break on the diaphyseal fragment a small exposed fresh break (roughly 6.5mm long) at the superior end of the *M. pectoralis major* insertion scar indicates recent detachment of a small flake of cortical bone.

The shaft fragment (U.W. 88-42) is 183mm long proximodistally (PD). Surface abrasion and exfoliation of small pieces of subperiosteal bone mar the anteromedial surface of the proximal shaft (in the area of the *M. latissimus dorsi* insertion). The posterior surface of the proximal break has a V-shaped area of missing bone that securely receives the most distally-projecting part of the shaft of the proximal fragment. A large crack originates from this notch, following the long axis of the shaft distally, and ultimately spiraling from the posterior to the medial surface at the supra-

Figure 5. MH1 right (U.W. 88-34, -42, & -88) and left (U.W. 88-36) humeri in anterior, lateral, posterior, and medial views (scale bar in cm).

condylar crest before returning back to the posterior surface where it terminates roughly 19mm above the most superior aspect of the olecranon fossa. The crack is filled with matrix, which has wedged the shaft open slightly, more so distally than proximally (thus midshaft and mid-distal diaphyseal diameters and circumferences are likely to be inflated by 2–2.5mm). Numerous hairline fractures are concentrated on the lateral surface of the distal diaphysis, following the long axis of the shaft, while they are less prevalent on other aspects of the diaphysis. Two hairline cracks also encircle the shaft (at about midshaft and about 20mm below midshaft). The proximal end of the lateral supracondylar crest is slightly abraded. A number of small (<3mm diameter) flakes of subperiosteal bone are missing from the dorsal surface of the bone above the olecranon fossa; based on the color of the underlying cortical bone these appear to be recent detachments (e.g., mining or excavation damage). The distal shaft is transversely fractured through the olecranon fossa, separating it from the distal fragment. The distal fracture exposes cancellous bone infilled with matrix over much of its surface, as well as having some matrix adhering to the broken cortical bone surface. The diaphyseal fragment preserves the superior 5mm of the lateral epicondyle and the superior corner of the olecranon fossa.

The distal fragment (U.W. 88-88) has a maximum SI dimension (26.1mm) laterally (at the middle of the capitulum) and an ML dimension of 51.5mm. The medial epicondyle is unfused, but the capitellar/lateral trochlear, medial trochlear, and lateral epicondylar secondary ossification centers were fused at the time of death. The metaphyseal surface for the medial epicondyle appears as a round pit 7.9mm in diameter and 2.2mm deep. The proximal fracture surface of the distal fragment exposes cancellous bone infilled with matrix, as well as areas with matrix adhering to broken cortical bone surfaces. A thin septum of matrix separates the olecranon fossa from the coronoid fossa, making it difficult to determine the presence or absence of a supratrochlear foramen (septal aperture). However, examination of the dorsal side of this matrix wall under magnification reveals the broken edges of a thin layer of cortical bone, denoting the presence of what appears to have been a bony septum in life (thus a lack of a septal aperture in this individual).

The anterior and inferior surface of the capitulum is mildly abraded and pitted, as is the anterior surface of the lateral trochlear keel. The anterior portion of the medial trochlear keel has been planed off in a coronal plane, exposing a 9mm (SI) by 6.4mm (ML) patch of trabecular bone (with matrix infilling). The medial trochlear keel is abraded along its entire preserved circumference, with a second small patch of cancellous bone (ca. 4mm in diameter) exposed on its inferior surface. A thin layer of matrix adheres to the posteromedial corner of the medial keel. A moderately large piece of matrix (13.5mm by 10.5mm) is stuck to the distal humerus, on the anteroinferior margin of the fusion site for the medial epicondyle apophysis.

Morphology. Although the MH1 right humerus lacks its proximal epiphysis, maximum length can be estimated by reference to the size of the articular surface of the head in the comparably-sized individual MH2. Virtual clearing of matrix and refitting of the three portions of the humerus produces a combined length (without the proximal epiphysis) of 240mm. The distance from the inferior-most lip of the metaphyseal surface (on the posterior surface) to the level of the distal capitulum (taken parallel to the shaft axis) of the virtual model is 223mm. The distance from the inferior-most articular margin of the right side humeral head of MH2 (on the posterior aspect) to the superior surface of the head (taken parallel to the shaft axis) is 25mm, producing an estimated maximum length of 248mm for the MH1 humerus. Alternatively, maximum humeral length was estimated from the preserved shaft and distal end using regression equations from modern human humeri provided by Steele (1970). The resulting length estimate (which is expected to overestimate the actual length, since the reference sample is of larger size than MH1) is 253.7±2.5mm (mean estimate and standard error of the estimates from six population and sex specific regression equations in Steele [1970]). Thus the maximum length of the MH1 humerus was likely between about 248 and 259mm, but probably towards the lower end of that range.

Based on the proximal metaphysis, the humeral head is posteriorly directed and thus the humeral torsion angle is low (estimated at 12° by Churchill et al. [2013]). The preserved portion of the unfused metaphysis has the typical irregular, convoluted appearance common to bone underlying metaphyseal growth plates. The metaphysis of the humeral head measures 30mm AP; the ML dimension cannot be determined due to damage. Maximum neck diameter is 21.7mm, and the minimum diameter is 18.1mm. Circumference of the surgical neck is 62.5mm.

The bicipital sulcus is broad (measuring 12.9mm from the lateral to the medial lip of the intertubercular groove at the proximal end), but also shallow (1.6mm deep at its deepest point). The crest for the *M. pectoralis major* insertion is strongly projecting, wide (ca. 7mm near its distal end), and rugose. At the proximal break, the diaphysis is mediolaterally elongate and oval in shape (except for the projecting *M. pectoralis major* crest). Surface damage precludes evaluation of the surface morphology of the *M. latissimus dorsi* insertion. A faint line of rugosity marks the *M. teres major* attachment on the medial mid-proximal shaft. A mildly rugose area on the posterolateral aspect of the mid-proximal shaft (at the very proximal end of the diaphyseal fragment) marks the origin of the lateral head of *M. triceps brachii*. The deltoid tuberosity is prominent, moderately rugose, and extends about 10mm distal of midshaft. The deltoid tuberosity is anterolaterally positioned, rather than the more lateral position seen in modern humans. The more anterior placement of the *M. deltoideus* insertion compared to modern humans is likely a secondary consequence of the low torsion angle (see Carretero et al. 1997). Diaphyseal shape in the mid-proximal to midshaft region is dominated by the deltoid tuberosity, and distal of midshaft the anteroposterior diameter rapidly decreases. Posterior to the insertion for *M. deltoideus* the radial sulcus is weak but palpable.

The midshaft maximum external diameter (M-5) is

19mm, the minimum diameter is 13.7mm, and circumference is 55.5mm (these values are uncorrected for the expansion to the shaft created by the longitudinal fracture on the posterolateral surface). The superior aspect of the nutrient foramen is visible 86.2mm distal to the proximal break on the medial side, but most of the foramen is obscured by a small amount of matrix adhering to the diaphyseal surface. At midshaft, the diaphysis is a skewed oval in its periosteal contour (with the long axis running anterolateral-posteromedial). Origination areas of *M. brachialis* and the medial head of *M. triceps brachii* are smooth and featureless, as is the insertion site of *M. coracobrachialis*. The distal minimum shaft circumference (M-7) is 50mm. Because of the strong development of the lateral supracondylar crest, minimum shaft circumference is located just below the deltoid tuberosity, rather than in the mid-distal shaft as exhibited by modern humans.

The lateral supracondylar ridge is thick (3.9mm AP at its midpoint) and rugose, and extends roughly 47mm proximal of the lateral superior-most point on the medial epicondyle. While the anterior surface of the shaft medial of the ridge is not especially rugose, size and projection of the ridge suggests hypertrophy of the *Mm. brachioradialis* and *extensor carpi radialis longus*. The lateral epicondyle is pronounced and rugose, and achieves its greatest lateral projection above (proximal to) the superior-most point on the anterior capitulum (that is, the lateral epicondyle is proximally positioned). The lateral epicondyle projects laterally 15.5mm from the lateral crest of the trochlea on the posterior surface. On the medial epicondyle, the origination site of the humeral origin of *M. pronator teres* is only mildly rugose. The biepicondylar breadth *without the medial epicondyle apophysis* is 52mm mediolaterally (adding an estimated 5mm for the missing apophysis provides a reasonable estimate of biepicondylar breadth of 57mm), and the medial epicondyle (again sans apophysis) projects medially 9.8mm from the medial trochlear margin. The olecranon fossa has a mediolateral dimension of 23.6mm at its widest point, and a maximum superoinferior dimension of 17mm. The approximate depth, relative to the medial and lateral corners and measured to the center of the fossa, is 6.5mm. The lateral pillar is 14.9mm thick, while the medial pillar is 9.6mm thick. The proximal edge of the olecranon fossa, which is visible on the shaft fragment, does not have a sharp apex superiorly, and is mediolaterally elongate and rounded.

The distal articular breadth (M-12a) is estimated at 37.7mm. The capitulum has a breadth (M-12) of 14.1mm, a SI diameter of 14.9mm and a circumference (maximum arc in the mid-sagittal plane of the surface) of 30mm. The capitulum is superoinferiorly elongated such that the distal-most aspect of the articular surface projects farther distally (by about 2.5mm) than the most distal point on the medial trochlear keel. The anterosuperior-posteroinferior diameter of the capitulum (measured across the articular surface) is 17.4mm, while the anterior projection (the AP diameter from the most projecting point on the anterior surface to the non-articular dorsal surface) is 17.5mm. The radial (supracapitellar) fossa is large, and is wider (ca. 13.7mm ML) than the coronoid fossa (ca. 9.4mm ML); both fossae appear tall (ca. 7.5mm) and deep relative to those of modern humans. The sulcus between the lateral trochlear ridge and the capitulum is relatively deep, producing a marked trochlear/capitellar keel. The trochlea is relatively small, such that the humeral cubital articulation is dominated by the capitulum. The trochlea has a deep waist, creating a distinct groove between the medial and lateral trochlear crests. The estimated trochlear breadth (M-11) is about 22mm mediolaterally. On the posterior surface, the lateral trochlear crest is oriented obliquely from proximolateral to distomedial.

U.W. 88-36: Left Proximal Humerus Fragment

Preservation. This fragment represents the proximal end of the left humerus of MH1, lacking the epiphysis for the humeral head and greater and lesser tubercles, but preserving the bicipital groove and medial and lateral lips of the intertubercular groove (see Figure 5). Distally the specimen is transversely fractured through the surgical neck. The fragment has a maximum length of 37.2mm, extending from the most proximal point on the metaphysis to the most distally projecting point on the diaphysis. The distal fracture surface is unevenly broken, with the shaft extending further distally on its posterior surface. The medullary cavity is occluded by matrix. Some slight abrasion is evident on the subperiosteal surfaces, but overall the surface preservation is quite good. Subperiosteal bone has been removed on the distal lateral shaft, exposing a square patch of underlying cortical bone roughly 8.3mm in width.

Morphology. The proximal epiphysis is unfused and missing, and the exposed surface has the irregular and convoluted surface typical of metaphyses. Based on the relationship of the long axis of the metaphyseal surface of the head to the bicipital groove, the humeral head would have been directed posteriorly were it preserved (and thus like the right side, the humeral torsion angle would be low). The metaphysis of the humeral head measures 34.5mm AP; the metaphyseal surface achieves its widest ML dimension, 28.4mm, across the anterior ends of its surfaces for the greater and lesser tubercles. Maximum neck diameter is 22mm, while minimum diameter is 18.1mm; circumference of the surgical neck is 67mm (note that because of preservation these dimensions are derived from slightly higher on the surgical neck than corresponding dimensions from the right side fragment U.W. 88-34).

The bicipital sulcus is broader than that of the right side (measuring 14.7mm from the lateral to the medial lip of the intertubercular groove at the proximal end), but equally shallow (1.6mm deep at its deepest point). The medial lip of the bicipital groove is sharper in the left side than right side fragment, whereas the reverse is true of the lateral lip.

HUMERUS OF MALAPA HOMININ 2 (MH2)

UW88-57: Complete Right Humerus

Preservation. The right humerus of MH2 is broken into three pieces—a 110mm long proximal portion which includes the head and the shaft down to the middle of the deltoid tuberosity; a shaft fragment with a maximum length of ca. 88mm which preserves the distal end of the deltoid tuberosity; and a distal portion with a maximum length of ca. 92mm (measured parallel to the shaft axis) which preserves the distal shaft, epicondyles, and cubital joint surfaces (Figure 6). The proximal and middle fragments are separated by a transverse fracture through the shaft. Although there is a small amount of irregularity to the broken edges (e.g., the anterior surface of the shaft extends approximately 3mm further distally than the posterior surface), the break is largely perpendicular to the shaft axis. Crushing is apparent on a ca. 16mm (SI) by 13mm (ML) area on the posterolateral surface of the middle fragment at the break. This damage has resulted in partial detachment of some of the cortical bone, as well as loss of cortical bone around the margins of the defect. Fracture surfaces can be seen to be congruous, and would likely appose cleanly if matrix in the endosteal cavity did not intervene. Virtual preparation of the fracture surfaces confirms that the surfaces rejoin cleanly (except in the area of crushing, where cortical bone has been lost). The middle and distal fragments remain joined together by matrix, although an anteriorward dislocation of the distal end of the distal fragment has created angular displacement between the two pieces (on the order of about 20º) in the sagittal plane. The area of the fracture between these two portions is comminuted, although the detached fragments of the diaphysis remain glued to the shaft by matrix. Four comminuted fragments are visible externally—a ca. 20mm (SI) by 14 (maximum AP) J-shaped fragment on the medial and posterior surface; a ca. 16mm (SI) by 11mm (ML) rectangular piece on the lateral side of the dorsal shaft (missing two small chips of subperiosteal bone along its inferior border); a ca. 13mm (SI) by 10mm (ML) rectangular fragment on the dorsolateral shaft (separated from the previously described fragment by a hairline fracture); and a ca. 10mm wide by 6mm high triangular section on the dorsolateral shaft. This last fragment exhibits some fresh fracture edges, as well as a fresh fracture line extending distally 13mm from its posteromedial corner. There is also a fresh fracture line along the anterior margin of the two laterally positioned fragments below it. These fresh fractures likely occurred during removal of the specimen from the matrix. The remainder of the fracture lines are matrix-covered, thus representing damage prior to recovery and preparation.

Surface morphology of the specimen as a whole is very well preserved. Small abraded areas are visible on the articular and diaphyseal surfaces, and the anterolateral surface of the proximal shaft displays patchy removal of a very thin layer of subperiosteal bone over a ca. 46mm (SI) area just lateral of the *M. pectoralis major* insertion. Hairline fractures can be found in places on the diaphysis, especially on the dorsal surface proximal of the olecranon fossa. Insect or snail damage (see Val et al. 2015) is also evident on the medial margin of the anterior surface of the distal shaft (ca. 25mm proximal of the top of the medial epicondyle). A small amount of subperiosteal bone, over an area of about 5mm by 5mm, has been chipped away from the medial corner of the coronoid fossa. Based on coloration, this appears to be recent damage, most likely incurred during preparation. Otherwise, the surface is free of defects and morphological detail is well preserved.

The distal articular surface overall is well preserved. A few small abraded areas (<3mm diameter) appear on the anterior surface of the capitulum, and an 8.6mm long portion of the anteromedial lip of the medial trochlear ridge has been abraded off (based on coloration, the damage appears to have occurred prior to fossilization). Beyond these small defects, the cubital surfaces are intact.

Morphology. Virtual preparation and refitting of the fragments provides a reconstructed humerus with a maximum length (M-1) of 269mm and an articular length (M-2) of 264mm. The humeral head is posteriorly directed, and thus the MH2 humerus has a low torsion angle (117°: Churchill et al. [2013]).

The humeral head is elliptical in dorsal view, with the long axis directed SI. The SI diameter of the head is 33mm, while head breadth is 31.8mm, corresponding with the maximum ML diameter of the articular surface. In a less retroverted modern human humerus, this dimension would be taken in the AP rather than ML direction. The mediolateral arc of the articular surface measures 46mm. The greater tubercle is large relative to the size of the humeral head. The superior surface of the tubercle (i.e., the insertion surfaces for *Mm. supraspinatus* and *infraspinatus*) exhibits moderate rugosity (namely, some relatively large projections on an otherwise smooth surface) and has a ML dimension of 25.7mm and a maximum AP dimension of 10.2mm. A vertically oriented, small rounded crest projects laterally from the greater tubercle at the insertion site of *M. infraspinatus*. The lateral lip of the intertubercular sulcus is strongly developed, attaining a thickness (ML) of 5.3mm near the top of the bicipital groove, suggesting a well-developed *M. pectoralis major*. The lateral lip continues distally as a distinct, prominent rounded ridge before narrowing into a sharp crest at the level of the surgical neck. The lesser tubercle is salient, but unlike the condition seen in modern humans, it projects more medially than posteriorly. The lesser tubercle has a length (taken from laterosuperior-to-medioinferior along the insertion area of *M. subscapularis*) of 13.7mm and a maximum dorsal projection of 8.6mm. The attachment area of *M. subscapularis* is largely smooth but has a few large rugose projections along its anteromedial margin. Overall, the tubercle gives the impression of a strongly developed *M. subscapularis*. Proximally, the medial lip of the intertubercular surface is formed by the lateral margin of the lesser tubercle. Below the level of the lesser tubercle, the medial edge of the bicipital groove is formed by a weak crest that intersects the middle of the lesser tubercle proximally. At its superior extent, the intertubercular sulcus is narrow (6.2mm posterolateral-to-anteromedial) and deep (3.7mm). Continuing distally, the medial lip of the sulcus (formed by the lesser tubercle) deflects medially, such that the sulcus widens markedly (to ca. 12mm at the distal end of the lesser tubercle). In dorsal perspective

Figure 6. MH2 right (U.W. 88-57) and left (U.W. 88-101) humeri in anterior, lateral, posterior, and medial views (scale bar in cm).

the greater and lesser tubercles can be seen to project farther laterally and medially, respectively, than the humeral head; the ML breadth across the most projecting points on the tubercles (and perpendicular to the shaft longitudinal axis) is 35.2mm.

Maximum neck diameter is 20.1mm, while minimum diameter is 17.2mm. Circumference of the surgical neck is 58mm. The insertion site for *M. pectoralis major* is well developed, beginning as a rugose yet thin (3.7mm ML) crest inferiorly and developing into a rounded prominent ridge proximally. At the distal extent of the bicipital groove, an area of moderate rugosity on the medial margin marks the insertion site for *M. latissimus dorsi*. The distal part of this attachment area is overlapped medially by a distinct ridge for the insertion of *M. teres major*. This ridge is approximately 28.5mm long and is bounded on its medial side by a narrow sulcus. In conjunction with the projecting flange on the distal scapular axillary border (see above), this ridge indicates hypertrophy of the *M. teres major*.

No indication of the origin of the lateral head of *M. triceps brachii* can be discerned on the posterolateral shaft. The deltoid tuberosity is moderately developed and only moderately rugose. The distal extent of the *M. deltoideus* insertion does not quite reach midshaft (falling about 2mm short of the midshaft level). The deltoid tuberosity occupies an anterolateral position, rather than the more lateral position seen in modern humans, likely a secondary consequence of the low torsion angle (see Carretero et al. 1997). Unlike the midshaft diaphyseal contour of the MH1 humerus, that of MH2 is not dominated by the deltoid tuberosity (the AP diameter of the diaphysis distal of midshaft does not change significantly until one reaches the level of the proximal lateral supracondylar crest). The radial sulcus of MH2 is slightly more distinct than that of MH1. Midshaft maximum diameter (M-5) is 17.7mm, while the minimum diameter (M-6) is 13.9mm, and circumference (M-7a) is 52.5mm. The shaft has a triangular cross-section over the entire length of the deltoid tuberosity until the midshaft (with the base formed by the two crests of the deltoid tuberosity and the apex lying on the posteromedial corner of the shaft).

The distal minimum shaft circumference (M-7) is 51mm. Because of strong development of the lateral supracondylar crest, minimum circumference occurs just below the deltoid tuberosity, rather than in the mid-distal shaft, as in modern humans. The nutrient foramen is located on the medial shaft roughly 15mm below midshaft (i.e., in the area of minimum circumference). Mild rugosity on the medial shaft, just distal of the nutrient foramen, may mark the insertion site of *M. coracobrachialis*. The origination area of *M. brachialis* is smooth and featureless. The dorsal medial surface of the distal shaft in the area of the origination of the medial head of *M. triceps brachii* is relatively smooth, although there is a low, thin SI-oriented ridge in the middle of this area.

The lateral supracondylar ridge extends proximally from the lateral superior-most point on the lateral epicondyle as a distinct and thick (3.6mm AP at its midpoint) ridge for 40mm, and then continues proximally another 30mm as a relatively sharp border between the anterior and posterior surfaces of the shaft. The *M. brachioradialis* origin exhibits moderate rugosity, while the *M. extensor carpi radialis longus* origin site is marked by a 14.9mm (SI) by 4.1mm (ML) sulcus adjacent to the distal portion of the ridge. The lateral epicondyle is pronounced and proximally positioned (it achieves its greatest lateral projection proximal to the superior-most point on the anterior capitulum), projecting laterally 15.1mm from the lateral crest of the trochlea on the posterior surface. On the medial epicondyle, the origination site of the humeral origin of *M. pronator teres* is only mildly rugose, as is the attachment site for the common flexor tendon. Biepicondylar breadth is 50mm, and the medial epicondyle is strongly projecting (extending medially 13.1mm beyond the medial trochlear margin). The medial epicondyle measures 12.9mm in a SI direction at its medial end. The olecranon fossa is rounded in shape, being constrained in its lateral development by a thick lateral distal pillar. The olecranon fossa has a mediolateral dimension of 19.6mm at its widest point, and a superoinferior dimension of 16.1mm. The olecranon fossa contains a large (9.8mm SI by 6.8mm ML) septal aperture (examination of the margins of the aperture under magnification reveal that it is a true feature, not an artifact of taphonomic or preparatory damage). The approximate depth of the olecranon fossa, relative to the medial and lateral corners and measured to the medial edge of the septal aperture, is 6.4mm. The lateral pillar is 14.1mm thick, while the medial pillar is 7.7mm thick. The proximal edge of the olecranon fossa, visible on the shaft fragment, does not have a sharp apex superiorly, and is mediolaterally elongate and rounded.

The distal articular breadth (M-12a) is 32.4mm. The capitulum has a breadth (M-12) of 12.3mm, a SI diameter of 15.1mm and a circumference (maximum arc in the midsagittal plane of the surface) of 29mm. The anterosuperior-to-posteroinferior diameter of the capitulum, if measured across the articular surface, is 16.9mm, while the anterior projection (AP diameter from the most projecting point on the anterior surface to the non-articular dorsal surface) is 16mm. The radial (supracapitellar) fossa is very large, and is wider (ca. 14.3mm ML) and taller (ca. 10.1mm SI) than the coronoid fossa (ca. 11.7mm ML by 8.7mm SI); both fossae appear deep. There is a marked trochlear/capitellar keel produced by a deep sulcus between the lateral trochlear ridge and the capitulum. As in MH1, the trochlea is relatively small, resulting in a cubital articulation that is dominated by a capitulum that is relatively SI expansive. The trochlea has a deep waist, creating a distinct groove between the medial and lateral trochlear crests. Estimated trochlear breadth (M-11) is 16.2mm. On the posterior surface, the lateral trochlear crest is oriented in a superoinferior direction.

UW88-101: Left Humeral Head

Preservation. This specimen was separated from the diaphysis at its anatomical neck, and thus preserves only the proximal articular surface and most of the greater and lesser tubercles (see Figure 6). Maximum SI dimension of the fragment is 35mm. None of the humeral neck is preserved. The fracture surface is biplanar—both planes have their long axis oriented SI, but the posterior portion of the surface lies largely in the coronal plane, while the lateral portion lies in a parasagittal plane (the two surfaces meet at an angle of approximately 135°). The fracture surface is covered in matrix that is intercalated with underlying trabecular bone. The articular surface is complete, since laterally the fracture encroaches on, but does not cross, the line of attachment of the joint capsule. There is slight abra-

Figure 7. MH1 right ulna (U.W. 88-3) in anterior, lateral, posterior, and medial views (scale bar in cm).

sion to the anterior surface of the lesser tubercle and some very slight abrasion to the superior surface of the greater tubercle (note: based on the low torsion angle observed in the right-side humerus, it is assumed that the humeral head was also directed posteriorly on the left side. Thus the anterior surfaces of the lesser and greater tubercles would correspond to the lateral surfaces in most modern human humeri). The specimen is uniformly whitish in color, which gives the impression of weathering, but with the exception of the minimal abrasion described above and a small amount of root etching on the articular surface, the surface preservation of the fossil is excellent.

Morphology. In every aspect, the proximal left humerus is a virtual mirror-image of the morphology seen in the U.W. 88-57 right humerus. As in that specimen, the head is elliptical in dorsal view (long axis directed SI). The SI diameter of the head is 33.7mm, while the head breadth (maximum ML diameter of the articular surface) is 32.4mm. The mediolateral arc of the articular surface measures 47mm. The greater tubercle is relatively large, with a superior surface that has an ML dimension of 26.7mm. Insertion surfaces for *Mm. supraspinatus* and *infraspinatus* exhibit moderate rugosity (that is, some relatively large projections on an otherwise smooth surface). Maximum AP dimension of the tubercle is 11.7mm. As in the right humerus, a vertically oriented, small rounded crest projects laterally from the greater tubercle at the insertion site of *M. infraspinatus*. The lateral lip of the intertubercular sulcus is thick (5.6mm ML near the top of the bicipital groove) and rugose, suggesting a well-developed *M. pectoralis major*. The lesser tubercle is salient, but projects more medially than posteriorly. The lesser tubercle has a laterosuperior-to-medioinferior length (taken along the insertion area of *M. subscapularis*) of 16mm and a maximum dorsal projection of 8.9mm. The attachment area of *M. subscapularis* is smooth posteriorly, but rugose along its anteromedial margin. Prominence and rugosity of the lesser tubercle suggests a strongly developed *M. subscapularis*. At its superior extent, the intertubercular sulcus is narrow (6mm posterolateral-to-anteromedial) and deep (4mm). The medial lip of the sulcus, which is formed by the lesser tubercle, deviates medially as it proceeds distally, such that the sulcus markedly widens distally. In dorsal perspective the greater and lesser tubercles can be seen to project farther laterally and medially, respectively, than the outline of the humeral head; the ML breadth across the most projecting points on the tubercles, and perpendicular to the shaft long axis, is 36.5mm.

ULNAE

ULNA OF MALAPA HOMININ 1 (MH1)

U.W. 88-3: Right Proximal Ulna

Preservation. The virtually complete proximal half of an ulna is broken transversely near midshaft (Figure 7). The proximal apophysis of the olecranon process is unfused and missing, leaving the exposed metaphyseal surface. Length of the preserved portion is 97.5mm. There are two separate cracks that encircle the diaphysis in a direction orthogonal to its long axis—the wider of the two cracks is approximately 68mm distal to the tip of the coronoid process; the other is comparatively very fine and is more proximal on the shaft, being approximately 40mm distal to the tip of the coronoid process. A small amount of matrix still adheres to the ventral surface of the bone at the level of the more proximal crack, while on the dorsal surface at the same level two small (ca. 5mm diameter) flakes of subperiosteal bone have been lifted slightly from the surrounding surface. The endosteal cavity at the distal break through the shaft is occluded with matrix.

The external surface of the bone is unweathered and the bone itself is well-mineralized. The medial articular surface of the coronoid process exhibits a small pit approximately 5mm ML by 1mm AP, which appears to represent postmortem abrasion. A small sulcus is present on the dorsal surface of the olecranon process, and within the sulcus trabecular bone is visible (there is matrix intervening between the trabeculae). This sulcus is in the subcutaneous area of the dorsal aspect of the olecranon process, and is approximately 5.4mm proximodistally by 1.2mm mediolaterally. A thin layer of matrix still adheres to the articular surface in the radial notch. Otherwise the surface is free of modification and morphological detail can be readily observed.

Morphology. The olecranon process is relatively narrow mediolaterally, and has a longitudinal axis that does not deviate from the longitudinal axis of the diaphysis. The olecranon process also does not reflect dorsally from the diaphyseal axis, as has been observed in apes (Drapeau 2008). The height of the olecranon (M-7; McH-9: here and throughout the text on the Malapa ulnae, McH-# refers to measurement numbers in McHenry et al. [1976]) is 20.2mm, while its length (M-8; McH-12) (minus the missing proximal apophysis) is 12.7mm. Olecranon depth (McH-7) is 14.9mm. The olecranon has a breadth (M-6) of 19.2mm, while the breadth of the articular surface for the humeral trochlea is slightly narrower (18.9mm). A distinct tubercle for *M. flexor carpi ulnaris* projects medially from the proximomedial border of the olecranon, and based on its position it looks as if it would have continued proximally onto the olecranon apophysis. A pronounced *M. flexor carpi ulnaris* tubercle is present (SEC personal observation on original fossils) in the *Au. africanus* specimens StW 380, StW 398 and StW 431 (the latter has an especially prominent tubercle), while a more moderate tubercle is present in StW 113. In *Au. afarensis*, the development of the tubercle ranges from moderate in A.L. 438-1 (based on description in Drapeau et al. [2005]) to weak in A.L. 288-1 (SEC personal observation on cast). The insertion scar of *M. anconeus* extends from the proximolateral corner of the dorsal olecranon process, distally for an extent of ca. 52mm. Along its proximal medial border it is separated from the subcutaneous surface of the dorsal olecranon by a raised, rugose arching crest, roughly 18mm long PD. The insertion area is mildly rugose. Distally, the anterior margin of the insertion area is marked by an irregular, thin crest running distodorsally from the distal end of the *M. supinator* crest. Along its anteroproximal margin, below the articular surface of the trochlear notch, the *M. anconeus* insertion margin is formed by a proximodistally running pillar. Between this pillar and the articular surface at the 'waist' of the notch lies a relatively deep (ca. 1mm), 12mm long proximodistally oriented sulcus. The sulcus is bounded anteriorly by the lateral margin of the articular surface of the notch and distally by the posteroproximal corner of the radial notch. The sulcus measures approximately 2.5mm in its AP dimension. The pillar appears to represent the anteroproximal margin of the insertion of *M. anconeus*. The sulcus does not appear to be related to the origin of *M. supinator* (whose line of attachment does not appear to extend proximally beyond the radial notch), and likely represents the attachment site of the annular and radial collateral ligaments and, via the collateral ligament, *M. extensor carpi radialis brevis*.

On the medial surface, and extending proximally onto the olecranon process, there is a large shallow fossa excavated from the proximal ulnar diaphysis. The fossa is approximately 21.5mm PD and approximately 8.5mm AP. The fossa appears to be a consequence of well-developed muscle and ligament attachments adjacent to the fossa. Proximal and dorsal margins of the fossa are delimited by the tubercle for the ulnar contribution of *M. flexor carpi ulnaris* and a prominent crest for the posterior and oblique bands of the ulnar collateral ligament, respectively. The proximoventral margin of the fossa is formed by the rim of the articular surface in the trochlear notch. The distoventral margin is a small crest for the anterior band of the ulnar collateral ligament and the humero-ulnar head of *M. flexor digitorum superficialis*, which continues from the medial edge of the ulnar (brachial) tuberosity in a proximal and ventral direction onto the distomedial surface of the coronoid process. Modern humans tend not to have a similarly distinct excavation in this location, rather they tend to have a flat extension of the proximomedial diaphyseal surface into this area with the possibility of raised, rugose muscle attachment sites for *Mm. flexor digitorum superficialis* and *flexor digitorum profundus*. The ulnar attachment site for *M. flexor digitorum superficialis* in humans tends to form a triangular, rugose area at the distomedial corner of the coronoid process. This feature is absent in U.W. 88-3, which exhibits an incipient crest instead. *Pan*, by comparison, tends to exhibit a fossa at this location resembling that of U.W. 88-3, and also tends to lack the triangular, rugose area on the coronoid process for the *M. flexor digitorum superficialis*.

The guiding ridge on the articular surface of the olecranon is indistinct compared to its obvious presence on the coronoid process. Overall the trochlear keel is mildly developed and indistinct. The coronoid process has a height (McH-8) of 23.8mm. It has a maximum mediolateral dimension, as measured from the proximal margin of the radial notch to the medial margin of the articular surface for the humeral trochlea, of 17.7mm. While the trochlear keel overall is only mildly developed, its coronoid portion exhibits a distinct guiding ridge that partitions the articular surface into asymmetric medial and lateral regions. The medial portion has a maximum breadth of 11.6mm while the lateral portion has a maximum breadth of 8.2mm.

The trochlear notch is waisted, with a minimum breadth (McH-6) of 15.7mm, while the minimum breadth of the articular surface is 12mm (that is, the nonarticular strip commonly found on the medial margin in modern human ulnae penetrates only ca. 3mm into the notch). The trochlear notch chord (M-7(1); McH-10) is 17.6mm and the notch subtense (measurement S-4 in Solan and Day [1992]) is 7.7mm (as measured without the olecranon process apophysis). Although the proximal apophysis is missing, it is clear that the trochlear notch opens anteroproximally, as in chimps, living humans, and the Sterkfontein ulnae StW 113 and StW 398 (SEC personal observation) and probably, based on preserved morphology, StW 380 and StW 431. This differs from the generally more anteriorly oriented trochlear notches in the *Au. afarensis* specimens A.L. 288-1 (Johanson et al. 1982) and A.L. 438-1 (Drapeau et al. 2005), and in the *Homo erectus* specimen KNM-WT 15000 (SEC personal observation).

The ulnar tuberosity presents as a relatively non-rugose sulcus bounded by salient crests both medially and laterally. The sulcus measures approximately 16.6mm PD by 7.6mm ML. Ulnar tuberosity position (McH-11) is 29.1mm. The lateral crest is broad (approximately 3mm in width), projecting, and distinctly separates the ventral from the lateral aspect of the diaphysis. The insertion of *M. brachialis* is an oval-shaped depression facing anteromedially.

The radial notch is oval- to teardrop-shaped (tapering anteriorly) and shallow, measuring 8.5mm proximodistally and 12.3mm dorsoventrally. The notch is concave in both the proximodistal and dorsoventral directions. With respect to the shape of the notch, the distal margin is rounded while the proximal margin is vertical and straight. The anterodistal margin of the notch is continuous with a sharp crest running anteroproximally up the coronoid process for the anterior attachment of the annular ligament. The face of the notch is tilted slightly along its long axis (AP) from anteromedial to posterolateral, such that the notch faces superolaterally (at an angle of approximately 20–30° to the sagittal plane). The notch is also tilted slightly along its short (PD) axis from distolateral to proximomedial. The notch thus faces proximolaterally, at an angle of about 20º to the sagittal plane and long axis of the shaft. The proximal border of the radial notch is demarcated from the trochlear notch by a well-defined ridge, which creates a distinct beak at its dorsal termination.

A short crest is present at the attachment of the *M. supinator* that is not divided into proximal and distal portions. The crest is distinct and moderately rugose, but not particularly large—either in its lateral projection or its length (ca. 13mm PD). In most modern human ulnae, the supinator crest is continuous with the interosseous crest distally, while in most members of the genus *Pan*, the supinator crest lies dorsal to the level of the interosseous crest, and the two either do not meet, or intersect at an acute angle. In U.W. 88-3, the supinator crest, like that of chimpanzees, lies at a level slightly dorsal to that of the interosseous crest, and the two crests never meet. The ML diameter of the diaphysis at the level of the maximum development of the *M. supinator* attachment, but excluding the crest itself (that is, taken just posterior of the crest), is 12.4mm. The diameter with the crest included is 13.8mm.

The proximal shaft has an AP diameter (McH-13) of 13.9mm and an ML diameter (McH-14) of 11.8mm. The circumference at the same level (the distal end of the ulnar tuberosity) is 41.5mm. The interosseous crest is ill-defined. The crest is more rounded than sharp, and extends approximately 40mm proximal to the broken end. The diaphysis narrows in its ML diameter proceeding from proximal to distal. The ML diameter of the shaft at the distal break is 10.5mm, and the AP diameter at that level is 14.3mm. The virtual nonexistence of an interosseous crest combined with marked ML flattening of the shaft creates a D-shaped cross section with a flattened lateral surface at the broken end. The circumference at the distal break is 42.5mm. The nutrient foramen is visible on the anteromedial surface, approximately 63.5mm from the center of the trochlear notch.

ULNA OF MALAPA HOMININ 2 (MH2)

U.W. 88-62: Complete Right Ulna

Preservation. The right ulna of MH2 is complete (Figure 8). A crack (likely perimortem: L'Abbé et al. [2015]) separates the olecranon process, on the lateral side only, from the remainder of the shaft, and causes some angular displacement of the proximal end of the bone. The fracture line arcs from the trochlear articular surface near the tip of the coronoid process dorsally and proximally, widening as it goes. Where the fracture intersects the lateral margin of the trochlear notch it has attained a width of ca. 4mm SI. At this point, the crack traverses the dorsal surface of the bone, reaching a width of about 5.5mm PD before tapering off medially. The fracture is occluded with matrix along its length. This defect has resulted in a moderate medialward and a somewhat slighter anteriorward displacement of the olecranon process. Metrics of the proximal ulna were taken on an *in silico* reconstruction of the specimen by KJC, as described by Rein et al. (2017) (see Figure 9 for a rendering and for details of the reconstruction).

The shaft exhibits three transverse fractures—a fresh (post-fossilization) break at the approximate midshaft; a fresh break ca. 45mm distal of midshaft (mid-distal); and, a fresh break near the proximal end of the *M. pronator quadratus* crest (roughly 65mm distal of midshaft). The adjoining surfaces at each of these fractures appose cleanly, and have been repaired without impacting the length of the bone or the assessment of morphological detail. A 12mm (PD) by 6mm (AP) flake of subperiosteal bone has detached from the lateral side of the shaft near the distal end of the supinator crest, but still adheres to the bone close to its original position. At the midshaft fracture, a wedge-shaped piece of cortex has been slightly displaced, protruding a fraction of a millimeter above the surrounding subperiosteal surface. On the dorsolateral surface of the diaphysis at the mid-distal fracture, a small (5mm AP by 3mm PD) surficial layer of cortical bone has been lost (revealing freshly exposed bone underneath). A similar-sized but probably ancient (based on coloration) removal of cortical surface occurs 28mm distally, also on the dorsolateral surface. These appear to be the only defects in the specimen. Overall the surface morphology is in an excellent state of preservation.

Morphology. The maximum length (M-1) of the reconstructed ulna is 245mm. The length excluding the styloid process (McH-1) is 240mm, while the articular length (M-2) is 225mm (both measurements taken on the reconstructed ulna). The shaft is moderately bowed in the sagittal plane; in the coronal plane, the distal shaft (neck and head) is moderately laterally deflected.

Morphology of the proximal end of the bone is very similar to that seen in MH1. The olecranon process is mediolaterally narrow, with a breadth (M-6) of 17.4mm. The insertion site of *M. triceps brachii* is square in outline, 15.3mm ML by 16.2mm AP, and only mildly rugose. The surface at the insertion site lacks the fine striations seen on

Figure 8. MH2 right ulna (U.W. 88-62) in anterior, lateral, posterior, and medial views (scale bar in cm).

most modern humans at this location. Anterior to the *M. triceps brachii* insertion area the dorsal surface of the olecranon process deflects distally, creating a triangular surface that is 16.1mm (ML) wide at the base by 8.1mm (AP) high for the subtendinous bursa of the triceps muscle. The longitudinal axis of the process is aligned with the long axis of the diaphysis rather than being reflected dorsally, as has been observed in apes (Drapeau 2008). Olecranon process dimensions are as follows: height (M-7; McH-9)=20.7mm; length (M-8; McH-12)=16.7mm; AP diameter (McH-7)=14.4mm.

The trochlear notch is waisted, with a minimum breadth (McH-6: taken on the reconstructed ulna) of 15.8mm. Maximum ML dimension of the articular surface of the olecranon process is 17.4mm, and the minimum ML breadth of the articular surface in the trochlear notch is 12mm (measured on the reconstructed ulna). There appears to be little-to-no development of the nonarticular strip on the medial trochlear margin. The guiding ridge on the articular surface of the olecranon is indistinct, and it is only slightly better developed on the coronoid process. The coronoid process has a height (McH-8) of 24.8mm. It has a maximum medio-

Figure 9. Digital rendering of the reconstructed MH2 right ulna in anterior, lateral, posterior, and medial views. In silico reconstruction involved removing cracks (such as the crack in the trochlear notch) by segmenting and separating the parts bordering the cracks before repositioning them in anatomical orientation. Internal structure (such as trabecular struts) was used to align conjoining parts in orthogonal directions when possible. Reconstruction was performed in VGStudio Max 2.1 (Volume Graphics GmbH, Heidelberg, Germany).

lateral dimension of 16.9mm, as measured from the proximal margin of the radial notch to the medial margin of the articular surface for the humeral trochlea. A weakly developed trochlear keel divides the articular surface of the coronoid process into asymmetric medial and lateral regions, the former with a maximum ML breadth of 12mm and the latter with a maximum ML breadth of 5.1mm. Based on the reconstructed ulna, the trochlear notch chord (M-7(1); McH-10) is 18mm, and the notch subtense (measurement S-4 in Solan and Day [1992]) is 9mm. The trochlear notch opens anteriorly (see Figure 9), as in the *Au. afarensis* specimens A.L. 288-1 (Johanson et al. 1982), A.L. 438-1 (Drapeau et al. 2005) and KSD-VP-1/1 (Haile-Selassie et al. 2010), and in the *Homo erectus* specimen KNM-WT 15000 (SEC personal observation). This differs from the generally more anteroproximally oriented trochlear notches seen in chimps, living humans, and the Sterkfontein ulnae StW 113 and StW 398 (SEC personal observation) and probably, based on preserved morphology, StW 380 and StW 431.

The radial notch is teardrop-shaped (tapering anteriorly) and shallow, measuring 7.6mm PD and 12mm DV. The notch is concave in both the proximodistal and dorsoventral directions. As in the MH1 ulna U.W. 88-3, the outline of the radial notch is rounded distally and vertical and straight proximally. The anterodistal margin of the notch is continuous with a sharp crest running anteroproximally up the coronoid process for the anterior attachment of the annular ligament. The face of the notch is close to facing directly laterally, but there is a slight tilt to the notch along its short (PD) axis from distolateral to proximomedial, such that the notch thus faces slightly proximolaterally (at an angle of about 10° to the sagittal plane and long axis of the shaft). The proximal border of the radial notch is demarcated from the trochlear notch by a well-defined ridge, which creates a distinct beak at its dorsal termination.

On the proximal medial surface, a very large attachment area is evident for the ulnar contribution of *M. flexor carpi ulnaris* and likely also for the medial fibers of *M. triceps brachii.* A pronounced *M. flexor carpi ulnaris* tubercle is present in MH1, as well as in the *Au. africanus* specimens StW 380, StW 398, and StW 431 (the last of which has an especially prominent tubercle), while a more moderate tubercle is present in StW 113. In *Au. afarensis*, the development of the tubercle ranges from moderate in A.L. 438-1 (see Drapeau et al. 2005) to weak in A.L. 288-1 (SEC personal observation on cast). As in MH1, there is a large shallow fossa excavated from the medial surface of the proximal ulnar diaphysis, bounded proximally and dorsally by the tubercle for the ulnar head of *M. flexor carpi ulnaris*. The specimen also exhibits a prominent crest for the posterior and oblique bands of the ulnar collateral ligament, ventrally by the rim of the articular surface in the trochlear notch, and distoventrally by a small crest for the anterior band of the ulnar collateral ligament and the humero-ulnar contribution of *M. flexor digitorum superficialis*. This latter crest extends from a prominent tubercle on the distomedial surface of the coronoid process distally to form the medial edge of the ulnar (brachial) tuberosity. The fossa enclosed by the crest is approximately 20mm PD and approximately 9.3mm DV. Modern humans tend not to have a similar excavation in this location, instead typically having a flat extension of the proximomedial diaphyseal surface into this area with the possibility of raised, rugose muscle attachment sites for *Mm. flexor digitorum superficialis* and *flexor digitorum profundus*. The ulnar attachment site for *M. flexor digitorum superficialis* differs in MH1 and MH2—while the former has a small crest at this location, MH2 exhibits the common modern human morphology of a triangular, rugose area at the distomedial corner of the coronoid process.

On the proximal dorsal surface, the attachment area for *M. anconeus* begins at the proximolateral corner of the dorsal olecranon process and extends distally for ca. 62mm. Along its proximal medial border, it is separated from the subcutaneous surface of the dorsal olecranon by a raised, rugose arching crest, roughly 35mm long PD. The insertion area is mildly rugose, and as in MH1, its anteroproximal margin is formed by a distinct, PD oriented pillar, which is separated from the articular surface of the trochlear notch by a sulcus. The sulcus is bounded distally by the posteroproximal corner of the radial notch, and likely represents the attachment site of the annular and radial collateral ligaments and, via the collateral ligament, *M. extensor carpi radialis brevis*. Distally, the anterior margin of the *M. anconeus* insertion is marked by an irregular, thin crest running distodorsally from the distal end of the *M. supinator* crest.

The *M. supinator* crest is more strongly developed in MH2 than MH1. It is short (extending distally from the radial notch only about 15mm) but salient. It is not divided into proximal and distal portions. A low, rounded ridge connects the supinator crest with the interosseous crest distally, although the two crests are not lying in the same anteroposterior plane (the supinator crest is slightly dorsal of the interosseous crest), such that the connecting ridge joins the supinator crest at an acute angle. The configuration of this morphology is intermediate between that commonly seen in humans and that seen in chimpanzees (SEC personal observation). The ML diameter of the diaphysis at the level of the maximum development of the *M. supinator* attachment, but taken just posterior of and thus excluding the crest, is 12.8mm. Including the crest increases the diameter to 13.8mm.

The ulnar tuberosity lies in a deep furrow between a large, thick (maximum width ca. 4.5mm) lateral crest and low medial ridge. At its widest point the sulcus measures approximately 20mm PD by 6.3mm ML. The position of the ulnar tuberosity (McH-11) is 28.4mm. The lateral crest is broad, projecting, and distinctly separates ventral from lateral aspects of the diaphysis. The insertion of *M. brachialis* is of moderate rugosity, and faces anteromedially.

The proximal shaft has an AP diameter (McH-13) of 12.7mm, an ML diameter (McH-14) of 11.7mm, and a circumference of 39.5mm. The interosseous crest is sharp and somewhat prominent only for about 22mm of its proximal end. Further distally, the crest broadens as it becomes the rounded anterolateral corner of the shaft. Below midshaft the interosseous crest becomes somewhat more distinct, where it separates anterior and inferolateral surfaces of the shaft as a non-projecting crest. As in MH1, the diaphysis is D-shaped in cross-section from the level of the distal end of the supinator crest to the proximal end of the *M. pronator quadratus* crest. However, unlike the MH1 ulna, the flattened surface of the shaft faces dorsolaterally rather than directly laterally. The dorsal margin of the flattened surface is slightly roughened, marking the line of attachment of *Mm. abductor pollicis longus, extensor pollicis longus,* and *extensor indicis*. The ML diameter at midshaft is 8.8mm and the AP diameter (McH-5) is 11.8mm. This produces a midshaft flare (McH-4) value of -3mm, whose negative value reflects both the lack of development of the interosseous crest, and marked ML flattening of the shaft. The midshaft

Figure 10: MH1 distal right radius epiphysis (U.W. 88-12), in distal view (scale bar in cm).

circumference is 34mm. The nutrient foramen occurs on the anteromedial surface of the diaphysis approximately 67mm distal to the center of the trochlear notch.

Distally, the *M. pronator quadratus* crest is well developed, presenting as a thick (3mm) projecting crest spiraling from the anteromedial to the medial surface of the distal shaft over a distance of approximately 30mm. Maximum diameter of the shaft at the point of maximum projection of the crest is 9.9mm, while minimum shaft diameter at the same level is 7.9mm. Shaft circumference at this same location is 28.5mm. Distal minimum circumference (M-3) of the shaft is 27mm. The shaft deviates laterally at the level of the *M. pronator quadratus* crest, such that the neck and head sit slightly lateral to the long axis of the shaft.

Distal width of the head (McH-3) is 15.4mm (ML), while distal maximum depth (AP diameter of the distal epiphysis) is 16.4mm. The distal articular surface of the head of the ulna is a flattened half-ellipse, 15.4mm long (ML) across its base and 8.1mm high (AP). It is separated from the styloid process by a deep sulcus. The styloid process is prominent, measuring 6.6mm wide (ML) near its tip, and projecting about 5.5mm distal to the articular surface. The distal radial facet is narrow (maximum PD diameter=3.8mm) and uniformly wide from the medial to the lateral side of the head.

RADII

RADIUS OF MALAPA HOMININ 1 (MH1)

U.W. 88-12: Distal Epiphysis Of Right Radius

Preservation. This is an unfused epiphysis of a distal right radius (Figure 10). The proximal surface is obscured by matrix, ranging in thickness from a few millimeters to a centimeter. The fragment underwent removal of its dorsomedial corner (likely in antiquity, as the broken surface is covered in matrix), but most of the articular surface is present and is free of defects.

Morphology. The anterior margin of the articular surface is relatively distinct, although matrix obscures the lateral portion. The edges of the posterior surface are rounded and do not show a sharp delineation between articular and nonarticular surfaces. A rugose bump on the dorsal edge of the fragment appears in the area of the distal extent of the dorsal tubercle. The articular surface is concave in both ML and AP directions, and laterally the apex projects distally as it rises to meet the styloid process. There is no visible line or ridge separating the scaphoid and lunate facets.

Estimated distal breadth (M-5(6)) is 30mm. Carpal articular breadth is 23.5mm, measured as the maximum ML dimension of the articular surface. The AP dimension across the middle of the scaphoid facet is 9.8mm, while the estimated AP dimension across the middle of the lunate facet is 19mm (adding roughly 1mm for the missing dorsal margin). Although the ulnar facet is not preserved, its distal AP dimension can be estimated as 15mm from the preserved medial edge of the fragment.

RADIUS OF MALAPA HOMININ 2 (MH2)

UW88-85: Complete Right Radius

Preservation. The right radius of MH2 is complete (Figure 11). The specimen suffered a fresh transverse fracture, roughly at midshaft, during preparation. This fracture resulted in cleanly adjoining edges and the bone was repaired without alteration of length or morphology. The surface is marred by a number of very small defects, which include: 1) a fresh crack across the articular surface of the dorsal margin of the head; 2) an ancient (and likely perimortem: L'Abbé et al. [2015]) crack longitudinally through the radial tuberosity (with the loss of a triangular piece of bone 5mm high by 3mm wide at the base); 3) a transverse crack to the mid-distal shaft; 4) an area of slight crushing on the lateral surface of the mid-distal shaft, which includes uplifting of a 8mm long by 5.5mm wide piece of subperiosteal bone; and, 5) a fracture through the distal dorsal corner at the distal ulnar facet. Mild abrasion of the surface is visible in some areas, while hairline fractures can be discerned in others, particularly in the distal shaft. Otherwise the specimen is free of damage, and overall surface morphology is well-preserved.

Morphology. Maximum length (M-1) is 226mm, and articular length (M-2) is 220mm. The shaft is markedly bowed; the head and neck lie along a line connecting the ML midpoints of the proximal and distal joint surfaces, while most of the shaft (from just distal of the radial tuberosity to roughly the level of the proximal margin of the *M. pronator quadratus* attachment area) lies lateral of this line. Relative to an axis established by the head and neck, the distal articular surface is medially deflected 74° (the carpal articular surface faces distomedially).

The head is nearly round in proximal view, with an AP diameter (M-5(1)) of 18.8mm and an ML diameter (M-4(1)) of 17.8mm. Circumference around the head (M-5(3)) is 57mm. The fossa for the capitulum measures 12.3mm ML by 12.2mm AP, and is 1.5mm deep at its center. At the prox-

Figure 11. MH2 right radius (U.W. 88-85) in anterior, lateral, posterior, and medial views (scale bar in cm).

imal ulnar articular surface, the head is thin, measuring only 4.9mm PD on its medial side. With the exception of the dorsolateral margin of the radial head where the ulnar facet is vertically (PD) oriented, the ulnar articular surface is beveled such that it slopes inwards towards the center of the head proximally. In both chimps and humans, where beveled, the ulnar articular surface generally slopes in the opposite direction (SEC personal observation).

The radial neck is mediolaterally compressed, as is usually seen in *Pan* (but not *Homo*). The neck has an AP diameter (M-5(2)) of 11.4mm and an ML diameter (M-4(2)) of 7.9mm. The circumference at the middle of the neck (M-5(4)) is 32.5mm. The neck-shaft angle (M-7) is 14°. The radial tuberosity is medially directed, such that the interosseous crest, if projected proximally, would intersect the middle of the tuberosity and produce a position score of 3 (Trinkaus and Churchill 1988). The posterior margin of the tuberosity, along the attachment line of *M. biceps brachii*, is projecting and rugose. The anterior portion of the tuberosity (underlying the bicipital bursa) is smooth and featureless. The tuberosity has a PD length of 27.7mm and an AP breadth of 13mm. At the level of maximum development of the tuberosity, the shaft has a diameter (including the tuberosity) of 13.7mm (AL-PM). The minimum shaft diameter, which also occurs in the AL-PM direction, is 9.9mm just distal to the tuberosity. Radial head-neck length (M-1A) is 27.3mm. The medial margins of the *M. supinator* insertion area are smooth and undefined; slight rugosity marks the lateral margin of the supinator attachment site.

The proximal shaft is round in cross-section, with AP and ML external diameters of 10.3mm and 10.2mm, respectively. Circumference of the proximal shaft is 33mm. On the anterior surface there is a low, rounded ridge, roughly 30mm long PD, in the area of the oblique line for *M. flexor digitorum superficialis*. A thin and shallow but slightly roughened sulcus follows along the medial side of this ridge, likely demarcating the lateral line of attachment of *M. flexor pollicis longus*. The interosseous crest is poorly developed, and is really only clearly visible (and slightly projecting) at its proximal end. At this point (the crest's maximum development), the AP diameter (M-5) is 9.6mm and the ML diameter (M-4) is 11.1mm.

The diaphysis is ovoid in its midshaft cross-section, with an AP external diameter (M-5a) of 9.9mm and an ML external diameter (M-4a) of 11.3mm. Midshaft circumference (M-5(5)) is 33mm. The insertion site of *M. pronator teres* is relatively smooth and featureless. On the dorsal surface of the shaft, a low rounded ridge runs proximally from midshaft for approximately 25mm, perhaps demarcating the lateral line of origin of *M. abductor pollicis longus*. This ridge ends at midshaft, leaving no visible indication of the *M. extensor pollicis brevis* attachment.

Distal minimum circumference (M-3) is 33.5mm. The insertion area of *M. pronator quadratus* is smooth and featureless. The insertion of *M. brachioradialis* is pronounced, presenting as a 26.5mm PD crest along the anterolateral corner of the distal shaft. This crest is rugose and thick (ca. 3.3mm) and becomes increasingly salient distally, creating a distinct sulcus for the tendons of *Mm. abductor pollicis longus* and *extensor pollicis brevis*. On the dorsal surface of the distal shaft, a prominent crest beginning at the dorsal edge of the styloid process and extending proximally, separates the sulcus for the tendons of the short extensor and long abductor of the thumb from the sulcus for the tendon of *M. extensor carpi radialis longus*. A very low ridge separates this latter groove from that for the tendon of *M. extensor carpi radialis brevis*. The dorsal tubercle is prominent along the lateral side of a long sulcus for *M. extensor pollicis longus*. The adjacent groove for *Mm. extensor digitorum* and *extensor indicus* is poorly developed. The ML breadth of the distal epiphysis (M-5(6)) is 26mm, while its maximum AP depth is 19.5mm.

The anterior margin of the distal articular surface is sharp and distinct, as is the medial two-thirds of the posterior margin. The lateral portion of the posterior edge, however, is rounded and does not sharply delineate the articular and nonarticular surfaces. The distal articular surface is concave in both ML and AP directions, while laterally the apex projects distally to meet the styloid process. There is no visible line or ridge separating the scaphoid and lunate facets.

Carpal articular breadth (the maximum ML dimension of the articular surface) is 21.8mm. The AP dimension across the middle of the scaphoid facet is 10.1mm, while the AP dimension across the middle of the lunate facet is 14.8mm. The AP dimension of the ulnar notch (at its distal end) is 12.6mm. Areas of slight abrasion have removed the proximal margin of the articular surface of the ulnar head, but its PD dimension at the anterior end is 3.8mm. In addition, there is a medialward inflection of the distal third of the radial shaft (beginning at the location of some slight damage to the shaft, although the inflection does not appear to be caused by the taphonomic damage) which results in a medial inclination of the carpal articular surface. This inflection of the radial component of the radiocarpal joint is consistent with a more distally oriented scapholunate articulation and attendant distomedial rotation of the scaphoid (Kivell et al. 2018). The functional significance of this arrangement, if any, is uncertain.

COMPARATIVE MORPHOLOGY

Aspects of the comparative morphology of the shoulder and upper limb of *Au. sediba* have been presented elsewhere (Churchill et al. 2013; Ibáñez-Gimeno et al. 2017; Macias 2015; Rein et al. 2017). Here we augment that work with additional comparisons of the pectoral girdle, arm, and forearm of Malapa Hominins 1 and 2. Given the recent recovery of partial scapulae of several specimens of the genus *Australopithecus* (*Paranthropus*) besides MH2, namely KSD-VP-1/1 (Haile-Selassie et al. 2010; Melillo 2016), DIK-1-1 (Alemseged et al. 2006), and KNM-ER 47000 (Green et al. 2018), as well as the renewed analytical attention to the australopith shoulder that these specimens have engendered (Green 2013; Green and Alemseged 2012; Melillo 2011, 2015; Young et al. 2015a,b), we emphasize comparative scapular morphology and provide a new morphometric analysis of the scapula. Additional analyses of other aspects of upper limb morphology in *Au. sediba* are in preparation.

MATERIALS AND METHODS

Scapular morphometric data were collected on adult modern humans (*Homo sapiens*), great apes (*Pan troglodytes*, *Gorilla gorilla*, and *Pongo pygmaeus*), lesser apes (Hylobatidae), and fossil hominins (Table 1). The modern human sample was derived from both prehistoric Native American agriculturalists and from recent industrialized populations. The ape sample included both mountain (*G. g. beringei*) and western lowland (*G. g. gorilla*) gorillas; most of the gibbons were *Hylobates lar* (see also Green 2013) (see Table 1). In addition to MH2 (*Au. sediba*: using the scapula as reconstructed in Churchill et al. [2013]), the fossil scapulae included in the comparative sample have been assigned to *Au. afarensis* (A.L. 288-1 [data from high quality cast] and KSD-VP-1/1 [data from Haile-Selassie et al. 2010; Melillo 2011, 2016; and personal communication of S.M. Melillo to DJG), *Au. africanus* (Sts 7 and StW 162 [data for both specimens from originals]), *Au. (Paranthropus) boisei* (KNM-ER 47000; [Green et al. 2018; data from original]), *H. erectus* (KNM-WT 15000 [data from original]), *H. floresiensis* (LB6/4 [data from Larson et al. 2009; and personal communication of S.G. Larson to DJG), and *H. naledi* (U.W. 101-1301 [data from original]). While all of these fossils entered into univariate and bivariate comparisons presented below, most were not complete enough to be included in the multivariate analysis (see be-

TABLE 1. EXTANT HOMINOID SAMPLE SIZE FOR SCAPULAR MORPHOMETRIC ANALYSIS.

Taxon	Individuals
Pan troglodytes	94
Gorilla gorilla	114
Homo sapiens	86
Pongo pygmaeus	49
Hylobates	182

low).

Twelve three-dimensional scapular landmarks were collected by one of us (DJG) with an Immersion MicroScribe G2 digitizer (Figure 12, Table 2). Landmark data were used to calculate scapular lengths, indices, and angles (Table 3). Following Green (2013), angles were derived in three dimensions using R (Ihaka and Gentleman 1996) by calculating the intersection of two lines in space (i.e., four points) by first defining a plane on the scapula with three points (the superior and inferior angles and the intersection of the spine and vertebral border) and then projecting two lines within it to calculate their angle of intersection. Lateral expansion of the subscapularis fossa was measured with sliding plastic digital calipers. One-way ANOVA was used to evaluate scapular shape differences across extant taxa. Post-hoc Tukey HSD tests for uneven samples were used to evaluate significance of observed differences, given the large number of comparisons. All statistical analyses were performed in STATISTICA (StatSoft, 2014).

Principal components (PCA) and canonical variates analyses (CVA) of 18 linear and angular scapular measures were also performed on correlation matrices to assess gross multivariate scapular shape differences among the extant taxa, MH2, and KNM-WT 15000. Discriminant function analyses (DFA) additionally tested the probability that a given individual was (or was not) properly as-

TABLE 2. ANATOMICAL LANDMARKS ON THE SCAPULA.

1 - **Suprascapular notch –** the inferior-most point of this notch

2 - **Superior angle –** the superior-most point of the scapula with the superior and inferior angles falling on a line parallel to an imaginary vertebral column

3 - **Point of spine that meets vertebral border** (a straight line from the spinoglenoid notch to the medial edge of the spine was used if the spine diminished before intersecting with the vertebral border)

4 - **Inferior angle** - the inferior-most point of the scapula with the superior and inferior angles falling on a line parallel to an imaginary vertebral column

5 - **Infraglenoid tubercle –** inferomedial to point 7, attachment site of *M. triceps brachii*

6 - **Spinoglenoid notch –** the point where the base of the spine meets the blade inferior to the junction of the spine and the acromion

7 - **Inferior-most point of glenoid**

8 - **Coracoid side of maximum glenoid width –** anterior-most point of fossa

9 - **Acromion side of maximum glenoid width –** posterior-most point of fossa

10 - **Superior-most point of glenoid**

11 - **Point of spine above spinoglenoid notch –** the union of the spine and the acromion

12 - **Distal most point on the acromion**

See also Figure 12.

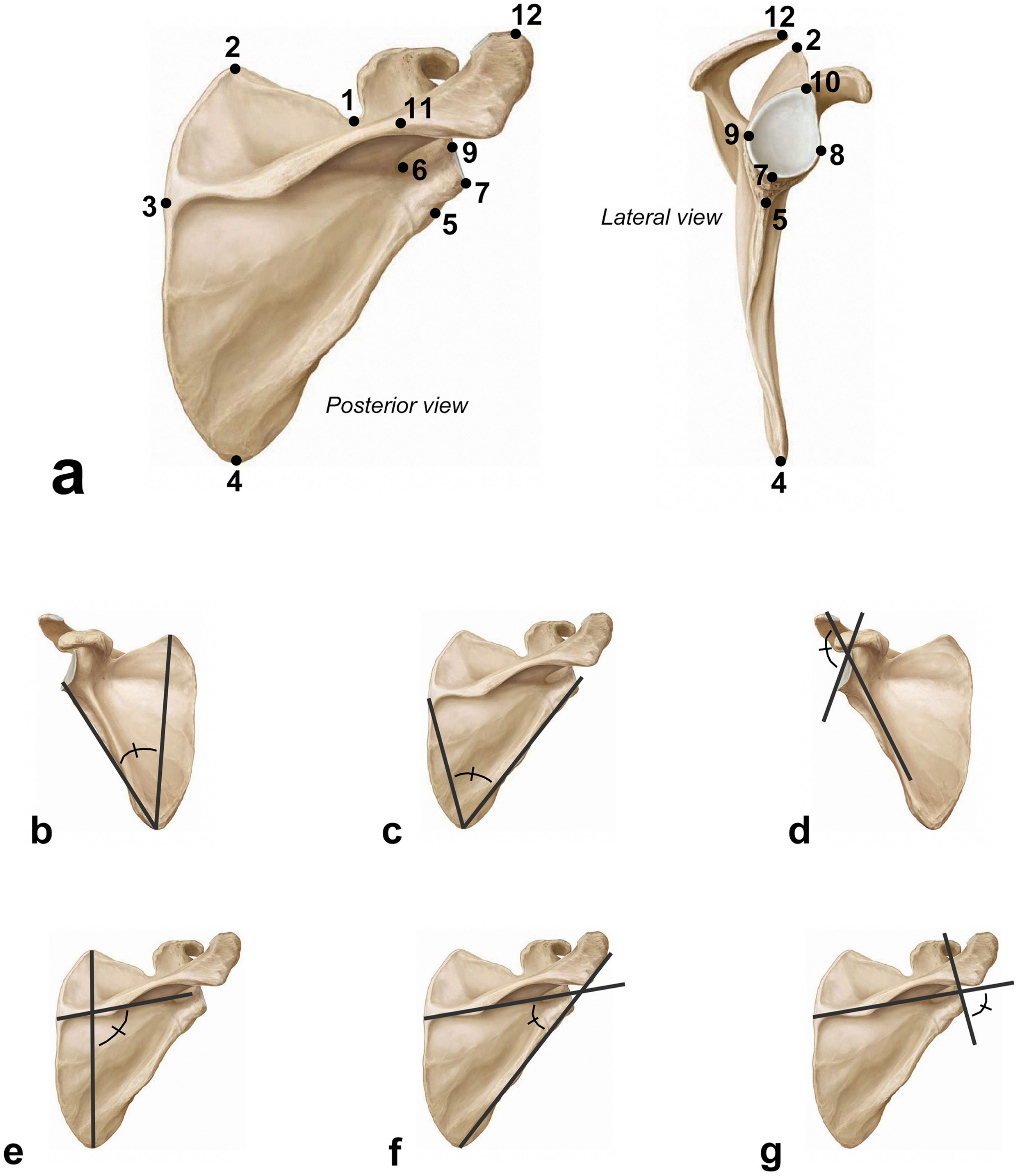

Figure 12. a) Scapular landmarks used in this study (image modified from Schuenke et al. 2007); see Table 2 for full list of landmarks. Depictions of the various angles considered here: b) axillary/medial border, c) axillary/infraspinous medial border, d) ventral bar/ glenoid, e) medial border/spine, f) axillary border/ spine, and g) spine/glenoid.

TABLE 3. LIST OF MEASUREMENTS USED IN THE SCAPULAR MORPHOMETRIC STUDY.

Measurement Name	Description
Axillary/medial border (AMB) angle	The angle formed by the medial (between landmarks 2 and 4) and axillary (between landmarks 4 and 5) borders
Axillary/infraspinous medial border (AIM) angle	The angle formed by the medial border and infraspinous breadth line (see below)
Ventral bar/glenoid (VBG) angle	The angle formed by the 'bar' of bone on the subscapularis fossa and glenoid height line
Medial border/spine (MBS) angle	The angle formed by the medial border and the base of the spine (between landmarks 3 and 6)
Axillary border/spine (ABS) angle	The angle formed by the axillary border and the base of the spine
Spine/glenoid (SPG) angle	The angle formed by the base of the spine and glenoid height line
Glenoid size	The square root of the product of glenoid height (landmarks 7-10) and width (8-9)
Total breadth	The distance between landmarks 2 and 4 (also used as the line for 'medial border')
Total length	The distance between landmarks 3 and 10
Spine length	The distance between landmarks 3 and 12
Superior border length	The distance between landmarks 2 and 12
Lateral expansion of subscapularis fossa	The perpendicular distance from landmark 5 to the ventral bar
Infraspinous breadth	The distance between landmarks 3 and 4
Infraspinous length	The distance between landmarks 4 and 6
Infraspinous neck width	The distance between landmarks 5 and 6
Supraspinous breadth	The distance between landmarks 2 and 3
Supraspinous length	The distance between landmarks 1 and 3

See also Table 2 and Figure 12 for depictions of landmarks and listed measures.

signed to their *a priori* group to assess the significance of group differences. An additional set of multivariate analyses were performed with fewer (11) variables in order to include KSD-VP-1/1, which is largely complete, save for much of the supraspinous fossa. All linear values were size-corrected by glenoid size to evaluate shape differences along the first two CV root axes. Using mean body masses derived from Smith and Jungers (1997), glenoid size scaled positively allometrically with respect to body mass across primates (x=1.13, r=0.97), suggesting that glenoid size may overestimate body size for larger-bodied individuals (e.g., male great apes). However, among great apes and humans, glenoid size and body mass scaled isometrically (x=1.00, r=0.89), suggesting it can be used confidently as a body size proxy among the taxa studied here.

COMPARATIVE MORPHOLOGY

Clavicular Morphology

Apes are characterized by a high scapular position with an obliquely-orientated clavicle, whereas modern humans have a low, dorsally-positioned scapula and horizontally-positioned clavicle (Larson 2007). These differences in scapular position have been functionally related to differences in relative clavicular length (Larson 2013) and curvature (Voisin 2006). The low claviculohumeral ratios of most extant apes (Larson 2013: the notable exceptions being *Pongo* and later *Homo*) suggests that relatively short claviculae may represent the primitive condition for hominoids. Claviculae of MH1 and MH2 appear relatively short in comparison to larger-bodied specimens such as the *Au. afarensis* clavicle KSD-VP-1/1f from Woranso-Mille (Haile-Selassie et al. 2010) and *Homo* (Churchill et al. 2013), reflecting more ape-like clavicular length proportions. While clavicular curvature in *Au. sediba* has not yet been quantified using Voisin's (2006) schema, the MH2 clavicle on visual inspection exhibits mild sigmoid curvature when viewed cranially. This is broadly similar in shape to the sigmoid curvatures of later *Homo* and *Pan* (Voisin 2006), though *Homo* has the more pronounced curvatures of the two. The reduced degree of sinuosity in the *Au. sediba* clavicle aligns it more with *Pan* than *Homo.* Functionally, the sigmoid curvatures of the human and chimpanzee claviculae provide greater leverage to *M. pectoralis major* during arm flexion, however, relatively straighter *Pan* claviculae demonstrate greater resistance to compressive and torsional forces exerted during locomotor behavior involving the forelimb, unlike the markedly S-shaped modern human clavicle (Harrington et al. 1993; Mays et al. 1999; Preuschoft et al. 2010). In dorsal view, both MH2 and MH1 claviculae have, on visual inspection, an inferior inflection at the acromial extremity and the shafts similarly inflect inferomedially. In the more complete MH2 specimen, this inferomedial inflection is also reflected in the orientation of the joint surfaces at the sternoclavicular joint (Churchill et al. 2013). *Au. sediba* appears to maintain two slight curvatures in dorsal view, unlike the single inferior (acromial) curve of later *Homo* claviculae that Voisin (2006) has associated with a low and dorsal scapula position characterizing modern humans. In this respect, *Au. sediba* appears more similar to the condition exhibited by extant great apes (dorsal curvature Group 1 in Voisin's schema).

Together these features (i.e., relatively short length and *Pan*-like appearance of clavicular curvatures, combined with a flanged conoid tubercle) evince a broadly ape-like pattern of clavicular morphology in *Au. sediba*, including an oblique orientation to the clavicle, and consequently indicate a scapula positioned high on the thorax. The cranially-oriented glenoid fossa of MH2 similarly supports the interpretation of shoulder positioning in *Au. sediba* as being more ape-like than human-like, implying continued recruitment of the upper limb in locomotor behavior and possibly some stabilizing selection for competence in—and biomechanical resistance to—over-head arm postures (Hunt 1991; Ward 2013).

Scapular Morphology

Summary statistics for scapular angles and shape ratios can be found in Table 4. In two angles that reflect overall shape of the scapular body—axillary/medial border (AMB) and axillary/infraspinous medial border (AIM) angles—MH2 was most similar to *Gorilla*. KNM-WT 15000 has a nearly identical AMB angle to MH2, reflecting a relatively narrow scapular blade in both fossils. However, while the MH2 AIM angle was most similar to that of *Gorilla*, both KNM-WT 15000 and KSD-VP-1/1 were most similar to *Pongo*. The scapula of MH2 is also ape-like in ventral bar/glenoid (VBG) angle, exhibiting a more cranially-oriented glenoid fossa and a VBG value very close to *Gorilla* and also *Pongo* means (Figure 13). Although VBG is an imperfect measure of the craniocaudal orientation of the scapular glenoid fossa (see Haile-Selassie et al. 2010)[1], it is interesting to note that scapular fossils of australopiths consistently tend to be more ape-like than human-like in this angle—A.L. 288-1 falls close to the *Pongo* mean, Sts 7 falls close to the *Pan* mean, StW 162 falls between the *Pan* and *Hylobates* means, and KSD-VP-1/1 and KNM-ER 47000 fall between the *Pongo* and *Homo* means (although KSD-VP-1/1 falls closer to *Pongo* and KNM-ER 47000 falls closer to *Homo*). Fossil specimens attributed to *Homo* are highly variable in VBG—U.W. 101-1301 had the lowest angle of the fossils, which actually matched the *Hylobates* mean; KNM-WT 15000 fell closest to the modern human mean; and, LB6/4 had an extremely laterally-oriented glenoid, well above the 95% confidence limits of the modern human sample (see Table 4).

With respect to orientation of the scapular spine (as measured by the medial border/spine [MBS] and axillary border/spine [ABS] angles), MH2 is again similar to *Pongo* (MBS) or intermediate between *Pongo* and extant *Homo* (ABS: see Figure 13). Alternatively, KNM-WT 15000 has a more horizontal spine that falls above the range of extant humans on ABS (see Figure 13). For ABS angle, both MH2 and A.L. 288-1 are intermediate between *Pongo* and modern humans, although the spine is more obliquely oriented in A.L. 288-1. Both KNM-ER 47000 and Sts 7 had *Gorilla*-like spine angles (see Table 4), while LB6/4 was virtually identical to the modern human mean. As with VBG angle, U.W. 101-1301 had the lowest ABS angle among the fossils, falling between the *Pan* and *Gorilla* means among the extant samples (see Table 4).

The angle formed by the scapular spine and the glenoid (SPG) was close to 90° for both *Gorilla* and *Pan*. Since the modern human average is just over 87°, it appears as though variation in the orientation of the glenoid within taxa, whether more transverse or more cranial, is matched by a spine that is more horizontally or obliquely oriented, respectively. Australopith scapulae including MH2, A.L. 288-1, KSD-VP-1/1, Sts 7, and StW 162 exhibited SPG angles that were in the lower 80° range, below African ape and modern human means but close to the *Pongo* mean. KNM-WT 15000 presents the lowest SPG angle value of all the fossils investigated here, which is even more remarkable given its relatively human-like VBG angle. This further highlights the extreme spine angle of KNM-WT 15000. Both KNM-ER 47000 and LB6/4 were close to 90°; these values are also unexpected given that KNM-ER 47000 combines an extremely oblique spine with a nearly human-like glenoid orientation, while LB6/4 displays a human-like spine orientation and a hyper-lateralized glenoid.

The MH2 scapula exhibits an absolutely small glenoid, about 3mm greater in size ($[AP*SI \text{ diameters}]^{0.5}$) than those of both A.L. 288-1 and LB6/4, but smaller than the means of all the hominids and all other hominins. KSD-VP-1/1 had the largest glenoid of the hominins considered in the present study, about 3mm larger than the mean of our modern human and *Pongo* samples, KNM-ER 47000, and StW 162 (see Table 4). Both Sts 7 and KNM-WT 15000 were intermediate between modern humans and *Pan*, but the juvenile status of KNM-WT 15000 is significant here—

TABLE 4. SCAPULAR SHAPE CHARACTERISTICS; ANGLE OR RATIO VALUE (95% confidence interval of the mean).

Axillary/medial border angle (°)	
Pan troglodytes	29.1 (28.7-29.5)[a]
Gorilla gorilla	34.1 (33.5-34.7)[b]
Homo sapiens	37.8 (37.0-38.6)[c]
Pongo pygmaeus	38.5 (37.4-39.5)[c]
Hylobates	32.8 (32.3-33.2)[d]
MH2	33.7
KNM-WT 15000	33.5
Axillary/infraspinous medial border angle (°)	
Pan troglodytes	42.2 (41.4-43.0)[a]
Gorilla gorilla	54.5 (53.7-55.2)[b]
Homo sapiens	51.4 (50.7-52.1)[c]
Pongo pygmaeus	46.1 (44.9-47.3)[d]
Hylobates	57.8 (56.7-58.9)[e]
MH2	55.8
KNM-WT 15000	47.5
KSD-VP-1/1[+]	46.9
Ventral bar/glenoid angle (°)	
Pan troglodytes	127.8 (126.8-128.7)[a]
Gorilla gorilla	130.6 (129.6-131.5)[b]
Homo sapiens	142.3 (141.0-143.5)[c]
Pongo pygmaeus	131.9 (130.1-133.7)[b]
Hylobates	121.1 (120.4-121.9)[d]
MH2	131.6
KNM-ER 47000A	138.4
KNM-WT 15000	137.6
LB6/4*	157.0
A.L. 288-1l	132.2
KSD-VP-1/1[+]	134.0
Sts 7	128.0
StW 162	124.3
U.W. 101-1301	121.1
Medial border/spine angle (°)	
Pan troglodytes	128.3 (127.3-129.3)[a]
Gorilla gorilla	115.7 (114.8-116.7)[b]
Homo sapiens	96.6 (95.5-97.7)[c]
Pongo pygmaeus	106.2 (104.1-108.3)[d]
Hylobates	137.2 (136.4-138.0)[e]
MH2	106.3
KNM-WT 15000	77.0

TABLE 4. SCAPULAR SHAPE CHARACTERISTICS; ANGLE OR RATIO VALUE (95% confidence interval of the mean) (continued).

Axillary border/spine angle (˚)	
Pan troglodytes	22.6 (21.7-23.5)[a]
Gorilla gorilla	30.1 (29.3-30.9)[b]
Homo sapiens	45.6 (44.5-46.7)[c]
Pongo pygmaeus	35.4 (33.6-37.1)[d]
Hylobates	10.0 (9.4-10.7)[e]
MH2	40.0
KNM-ER 47000A	29.1
KNM-WT 15000	69.6
LB6/4*	45.0
A.L. 288-1l	38.2
KSD-VP-1/1[+]	43.8
Sts 7	29.8
U.W. 101-1301	26.8
Spine/glenoid angle (˚)	
Pan troglodytes	91.3 (90.1-92.4)[a]
Gorilla gorilla	89.3 (88.5-90.1)[ab]
Homo sapiens	87.2 (86.1-88.3)[b]
Pongo pygmaeus	82.3 (80.7-84.5)[c]
Hylobates	96.9 (95.9-97.8)[d]
MH2	83.5
KNM-ER 47000A	90.9
KNM-WT 15000	68.2
LB6/4**	89.3
A.L. 288-1l	83.7
KSD-VP-1/1[+^]	80.6
Sts 7	83.4
StW 162	81.7
Glenoid size	
Pan troglodytes	26.7 (26.4-27.1)[a]
Gorilla gorilla	40.3 (39.3-41.3)[b]
Homo sapiens	29.8 (29.2-30.4)[c]
Pongo pygmaeus	30.7 (29.7-31.8)[c]
Hylobates	12.6 (12.5-12.8)[d]
MH2	23.3
KNM-ER 47000A	30.5
KNM-WT 15000	27.1
LB6/4*	19.5
A.L. 288-1l	20.8
KSD-VP-1/1[++]	33.8
Sts 7	28.8
StW 162	30.7

TABLE 4. SCAPULAR SHAPE CHARACTERISTICS; ANGLE OR RATIO VALUE (95% confidence interval of the mean) (continued).

Total breadth/glenoid size	
Pan troglodytes	5.74 (5.67-5.81)[a]
Gorilla gorilla	5.57 (5.50-5.64)[b]
Homo sapiens	5.10 (5.02-5.17)[c]
Pongo pygmaeus	4.52 (4.41-4.63)[d]
Hylobates	5.18 (5.12-5.23)[c]
MH2	5.32
KNM-WT 15000	5.76
Total length/glenoid size	
Pan troglodytes	3.97 (3.93-4.02)[a]
Gorilla gorilla	4.03 (3.99-4.08)[a]
Homo sapiens	3.50 (3.45-3.55)[b]
Pongo pygmaeus	3.48 (3.40-3.56)[b]
Hylobates	5.35 (5.27-5.43)[c]
MH2	3.66
KNM-WT 15000	3.41
LB6/4*	3.49
KSD-VP-1/1[++]	3.57
Total breadth/length	
Pan troglodytes	1.45 (1.43-1.46)[a]
Gorilla gorilla	1.38 (1.37-1.40)[b]
Homo sapiens	1.46 (1.44-1.48)[a]
Pongo pygmaeus	1.30 (1.27-1.34)[c]
Hylobates	0.98 (0.96-0.99)[d]
MH2	1.45
KNM-WT 15000	1.69
Spine length/glenoid size	
Pan troglodytes	5.00 (4.93-5.06)[a]
Gorilla gorilla	4.93 (4.85-5.01)[a]
Homo sapiens	4.40 (4.33-4.46)[b]
Pongo pygmaeus	4.19 (4.09-4.29)[b]
Hylobates	6.52 (6.43-6.61)[c]
MH2	4.45
Spine length/total length	
Pan troglodytes	1.26 (1.25-1.27)[a]
Gorilla gorilla	1.22 (1.21-1.24)[b]
Homo sapiens	1.256 (1.248-1.264)[a]
Pongo pygmaeus	1.21 (1.19-1.22)[b]
Hylobates	1.221 (1.216-1.225)[b]
MH2	1.22

TABLE 4. SCAPULAR SHAPE CHARACTERISTICS; ANGLE OR RATIO VALUE (95% confidence interval of the mean) (continued).

Superior border length/glenoid size	
Pan troglodytes	2.72 (2.67-2.76)[a]
Gorilla gorilla	2.91 (2.85-2.96)[b]
Homo sapiens	3.29 (3.21-3.37)[c]
Pongo pygmaeus	3.25 (3.17-3.34)[c]
Hylobates	3.65 (3.59-3.71)[d]
MH2	2.54
Superior border length/total length	
Pan troglodytes	0.68 (0.67-0.70)[a]
Gorilla gorilla	0.72 (0.71-0.73)[b]
Homo sapiens	0.94 (0.92-0.95)[c]
Pongo pygmaeus	0.94 (0.92-0.96)[c]
Hylobates	0.68 (0.67-0.69)[a]
MH2	0.69
Lateral expansion of the subscapular fossa/glenoid size	
Pan troglodytes	0.55 (0.53-0.56)[a]
Gorilla gorilla	0.52 (0.50-0.53)[a]
Homo sapiens	0.44 (0.43-0.46)[b]
Pongo pygmaeus	0.47 (0.44-0.49)[b]
Hylobates	0.68 (0.67-0.70)[c]
MH2	0.55
KNM-ER 47000A	0.51
KNM-WT 15000	0.54
LB6/4***	0.46
A.L. 288-1l	0.57
KSD-VP-1/1[++]	0.53
Sts 7	0.59
StW 162	0.55
Infraspinous breadth/glenoid size	
Pan troglodytes	3.09 (3.03-3.15)[a]
Gorilla gorilla	3.07 (3.02-3.12)[a]
Homo sapiens	3.74 (3.67-3.80)[b]
Pongo pygmaeus	3.33 (3.24-3.42)[c]
Hylobates	2.10 (2.04-2.16)[d]
MH2	3.81
KNM-WT 15000	4.75
KSD-VP-1/1[+]	3.99
Infraspinous length/glenoid size	
Pan troglodytes	5.35 (5.29-5.42)[a]
Gorilla gorilla	4.72 (4.65-4.78)[b]
Homo sapiens	4.44 (4.38-4.50)[c]
Pongo pygmaeus	4.66 (4.56-4.75)[b]
Hylobates	5.56 (5.50-5.62)[d]
MH2	4.75
KNM-WT 15000	4.31
LB6/4**	4.65
KSD-VP-1/1[++]	4.84

TABLE 4. SCAPULAR SHAPE CHARACTERISTICS; ANGLE OR RATIO VALUE (95% confidence interval of the mean) (continued).

Infraspinous breadth/infraspinous length	
Pan troglodytes	0.58 (0.57-0.59)[a]
Gorilla gorilla	0.65 (0.64-0.66)[b]
Homo sapiens	0.84 (0.83-0.85)[c]
Pongo pygmaeus	0.72 (0.70-0.73)[d]
Hylobates	0.38 (0.37-0.39)[e]
MH2	0.80
KNM-WT 15000	1.10
KSD-VP-1/1⁺⁺	0.82
Infraspinous neck breadth/glenoid size	
Pan troglodytes	0.78 (0.76-0.79)[a]
Gorilla gorilla	0.85 (0.83-0.86)[b]
Homo sapiens	0.90 (0.88-0.92)[c]
Pongo pygmaeus	0.81 (0.78-0.84)[ab]
Hylobates	0.96 (0.94-0.97)[d]
MH2	0.90
KNM-ER 47000A	0.69
KNM-WT 15000	0.87
LB6/4*	0.79
A.L. 288-1l	0.79
KSD-VP-1/1⁺⁺	0.64
Sts 7	0.78
StW 162	0.94
Supraspinous breadth/glenoid size	
Pan troglodytes	2.92 (2.86-2.98)[a]
Gorilla gorilla	2.90 (2.86-2.94)[a]
Homo sapiens	1.76 (1.72-1.80)[b]
Pongo pygmaeus	1.33 (1.26-1.41)[c]
Hylobates	3.52 (3.45-3.60)[d]
MH2	2.25
KNM-WT 15000	1.63
Supraspinous length/glenoid size	
Pan troglodytes	2.97 (2.92-3.02)[a]
Gorilla gorilla	2.99 (2.95-3.03)[a]
Homo sapiens	2.43 (2.39-2.47)[b]
Pongo pygmaeus	2.37 (2.30-2.44)[b]
Hylobates	4.22 (4.15-4.29)[c]
MH2	2.60
KNM-WT 15000	2.50
KSD-VP-1/1⁺⁺	2.68

TABLE 4. SCAPULAR SHAPE CHARACTERISTICS; ANGLE OR RATIO VALUE (95% confidence interval of the mean) (continued).

Supraspinous breadth/supraspinous length	
Pan troglodytes	0.98 (0.97-0.99)^{a}
Gorilla gorilla	0.97 (0.96-0.98)^{a}
Homo sapiens	0.73 (0.71-0.74)^{b}
Pongo pygmaeus	0.56 (0.54-0.59)^{c}
Hylobates	0.83 (0.82-0.84)^{d}
MH2	0.87
KNM-WT 15000	0.65
Supraspinous breadth/infraspinous breadth	
Pan troglodytes	0.96 (0.92-0.99)^{a}
Gorilla gorilla	0.95 (0.93-0.97)^{a}
Homo sapiens	0.47 (0.46-0.49)^{b}
Pongo pygmaeus	0.40 (0.38-0.43)^{b}
Hylobates	1.76 (1.69-1.83)^{c}
MH2	0.59
KNM-WT 15000	0.34

Differences between extant taxa was assessed by one-way ANOVA. Significant differences between adults were assessed using a post-hoc Tukey honestly significant difference test for multiple comparisons. Extant values with different superscript letters represent taxa that were significantly different at the $\alpha \leq 0.05$ level (e.g., *Pan* and *Gorilla* for axillary/medial border angle); taxa with the same superscript were not significantly different (e.g., *Homo* and *Pongo* for the same angle comparison). All comparative and fossil data was collected by DJG with following exceptions:

*Data from Larson et al. 2009, **estimated with ImageJ from Figure 13 of this reference, and ***S.E. Larson personal communication (to DJG).

$^{+}$Data from Melillo 2016 and $^{++}$S.M. Melillo, personal communication (to DJG), although the reported maximum glenoid size index of 33.8 (i.e., the square root of 39.0 SI multiplied by 29.3 AP) was used to calculate scapular neck breadth and subscapularis lateral expansion relative to glenoid size. The maximum glenoid size was more similar to the way it was measured in our comparative sample than Melillo's (2016) reported glenoid size value of 29, which represented only the articular surface.

$^{\wedge}$This measurement is the complement of the angle reported in Melillo (2016).

an adult KNM-WT 15000 glenoid fossa would have likely been closer in size to that of modern humans or even KSD-VP-1/1, since the juvenile's glenoid was just less than comparably-aged *Gorilla* and ~3mm greater than like-aged modern *Homo* (Green and Alemseged 2012). Again, scapular glenoid fossa size scales isometrically with body size in great apes and humans, such that the variation noted above is likely to be tracking variation in body size.

In terms of scapular breadth relative to glenoid fossa size, MH2 is intermediate between modern humans and *Gorilla*, while KNM-WT 15000 was within the 95% CI limits of the *Pan* mean (see Table 4). With respect to scapular length relative to glenoid fossa size, both MH2 and KSD-VP-1/1 are intermediate between the extant *Homo*/*Pongo* and *Pan* sample means, but outside the 95% CI limits of all three samples. Fossil *Homo* specimens KNM-WT 15000 and LB6/4 fall closer to the sample means for *Homo* and *Pongo* (see Table 4).

The MH2 spine was most similar in length (scaled to glenoid size) to modern humans. *Pan* and *Homo* had spines that were slightly longer relative to scapular length than the other taxa, but in general, spine length was consistently ~22–25% longer than total scapular length, even in MH2. KNM-WT 15000 was not considered in this analysis, as its acromion was not fully fused to the spine and was not recovered. Superior border length scaled to glenoid size in MH2 fell below all of the extant sample means, but when superior border length is scaled to total scapular length MH2 falls very close to the means of both *Pan* and *Hylobates* (see Table 4).

The *Pongo* and *Homo* samples had the narrowest relative (to glenoid size) expansion of the lateral margin of the subscapular fossa (as discussed in Larson [1995]); *Hylobates* had the widest subscapular lateral expansion of all taxa considered, while *Pan* and *Gorilla* were intermediate. Both MH2 and KNM-WT 15000 had relatively broad *M. subscapularis* lateral expansions that were within the *Pan* 95% CI limit. Similarly, other australopiths have relatively broad lateral expansions comparable to *Pan*. KNM-ER 47000 has a slightly narrower *M. subscapularis* lateral expansion that

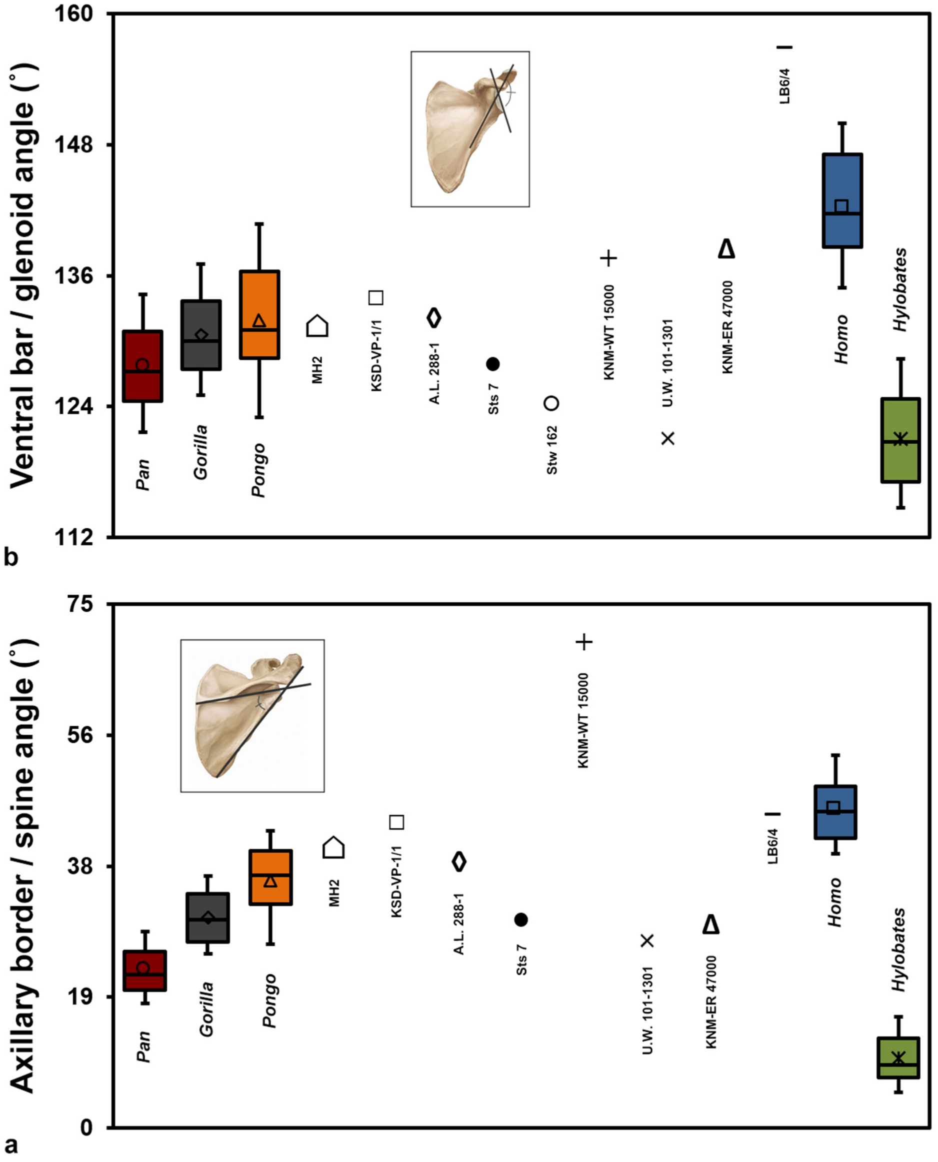

Figure 13. Box and whisker plots of a) axillary border/spine and b) ventral bar/glenoid angles across extant taxa and fossil individuals.”MH2, most of the australopith fossils, and Homo naledi *have more cranially-oriented glenoid fossae than those of modern* Homo*, while KNM-ER 47000 and KNM-WT 15000 display more laterally-oriented joints, comparable to those of modern* Homo*. MH2 and the East African australopiths fall between* Pongo *and* Homo *for this measure, while* H. naledi*, KNM-ER 47000, and Sts 7 had more angled spine orientations, like the African apes. Modern* Homo *and LB6/4 had more horizontally-situated spines, while KNM-WT 15000 possessed the most extreme example of this type of orientation. Boxes encompass the middle 50% of the data range, while the central line represents the median value, and the whiskers extend from the lower 10% to the upper 90% of samples.*

is within the 95% CI limit of the *Gorilla* mean. LB6/4 has the least expanded subscapular fossa of the fossil hominins, falling within the modern human range (see Table 4). Extant *Homo* had the superoinferiorly broadest infraspinous fossa relative to glenoid size, followed by *Pongo*, and with *Pan* and *Gorilla* possessing the narrowest infraspinous fossae of the great apes. *Hylobates* had even narrower infraspinous fossae compared to those of great apes, reflecting their extremely oblique scapular spine orientation. All of the fossils had human-like, broad infraspinous fossae, with KNM-WT 15000 being the most extreme. Modern human infraspinous fossae were the shortest mediolaterally, followed closely by *Pongo* and then *Gorilla*. *Hylobates* and *Pan*, on the other hand, had the longest infraspinous fossae. MH2 infraspinous length was most similar to *Gorilla*, as was KSD-VP-1/1, while LB6/4 was most similar to *Pongo* and KNM-WT 15000 was just below the lower bound of the 95% CI limit of modern humans. With both the broadest and shortest infraspinous fossa, *Homo* had the largest infraspinous breadth/length ratio of all the extant taxa considered, while *Hylobates* had the smallest ratio. *Pan* had the lowest ratio among the great apes, followed by *Gorilla* and

TABLE 5. VARIABLE LOADINGS FOR THE 18-VARIABLE PRINCIPAL COMPONENTS ANALYSIS.

	PC1	PC2	
Infraspinous breadth/length	-0.976	-0.804	Axillary/medial border angle
Axillary border/spine angle	-0.957	-0.599	Axillary/infraspinous medial border angle
Infraspinous breadth/glenoid	-0.916	-0.418	Infraspinous neck/glenoid
Total breadth/length	-0.825	-0.140	Total length/glenoid
Ventral bar/glenoid angle	-0.719	-0.122	Lateral expansion breadth/glenoid
Axillary/medial border angle	-0.420	-0.082	Supraspinous length/glenoid
Total breadth/glenoid	0.139	-0.061	Supraspinous/infraspinous breadth
Supraspinous breadth/length	0.311	-0.046	Ventral bar/glenoid angle
Infraspinous neck/glenoid	0.379	-0.014	Axillary border/spine angle
Axillary/infraspinous medial border angle	0.476	0.001	Spine/glenoid angle
Spine/glenoid angle	0.712	0.027	Infraspinous breadth/length
Lateral expansion breadth/glenoid	0.764	0.230	Medial border/spine angle
Infraspinous length/glenoid	0.779	0.232	Infraspinous breadth/glenoid
Supraspinous breadth/glenoid	0.911	0.302	Supraspinous breadth/glenoid
Medial border/spine angle	0.936	0.310	Infraspinous length/glenoid
Total length/glenoid	0.950	0.517	Total breadth/length
Supraspinous/infraspinous breadth	0.954	0.758	Supraspinous breadth/length
Supraspinous length/glenoid	0.963	0.855	Total breadth/glenoid

Pongo (see Table 4). Both MH2 and KSD-VP-1/1 had similar ratios to modern humans, while KNM-WT 15000 had what can only be considered a "hyper-human" value, based largely on its extreme infraspinous breadth.

Breadth of the infraspinous neck (relative to glenoid size) of MH2 is identical to the modern human mean. StW 162 exhibits a ratio that is intermediate between the extant *Homo* and *Hylobates* means, while KNM-WT 15000 falls between the *Homo* and *Gorilla* means. A.L. 288-1, Sts 7, and LB6/4 were within the *Pan* range of values, while KNM-ER 47000 was markedly narrower than the extant taxa and fossil individuals, with the exception of KSD-VP-1/1 (see Table 4). Breadth of the supraspinous fossa (relative to glenoid size) in MH2 is intermediate between the African apes and modern human means, and KNM-WT 15000 was most similar to extant *Homo.* The relative length of the fossa of all of the fossils were intermediate between modern humans and the African apes, with KNM-WT 15000 being most similar to modern humans (see Table 4). Among the extant samples, *Pongo* exhibits the lowest relative supraspinous breadth/length ratio, *Homo* is intermediate, and *Hylobates*, *Pan*, and *Gorilla* possess the largest ratios. *Pan* and *Gorilla* supraspinous fossae were notable for having breadths that were nearly equal to their lengths (and thus ratios close to one). The MH2 ratio was much higher than in modern humans and intermediate between *Hylobates* and the African apes. On the other hand, KNM-WT 15000 was intermediate between *Homo* and *Pongo* (see Table 4). The proportions of the supraspinous and infraspinous fossae distinguishes African apes from *Homo* and *Pongo* and reflects the gross differences in scapular shape between them. *Homo* and *Pongo* supraspinous fossae breadths were between 40–50% of that of the infraspinous fossa, while *Gorilla* and *Pan* had nearly equal supraspinous and infraspinous breadths. *Hylobates* present an opposite extreme, with supraspinous fossae nearly twice as broad as the infraspinous fossa. Both fossils trended closer to modern humans and *Pongo*—the ratio in MH2 was significantly greater than the mean of modern humans, but was certainly closer to it than the African apes, while the KNM-WT 15000 ratio was lower than even *Pongo* (see Table 4).

Two different sets of scapular metrics were used for separate multivariate considerations—one with 18 variables that considered all extant taxa, MH2 and KNM-WT 15000 (Table 5), and a second analysis with 11 variables to additionally include the slightly less complete KSD-VP-1/1 (Table 6). Both datasets were included in a principal components analysis as well as a canonical variates analysis to evaluate the significance of scapular shape differences among the extant groups (Tables 7 and 8). In the broader analysis using 18 variables, the first two principal component axes explained 76.7% of the sample variance. Along PC 1 (59.5% of the variance), *Hylobates* were shifted positively away from modern *Homo* and *Pongo*, while *Pan* and *Gorilla* fell intermediately along PC1, but were separated from the other extant groups by having more positive values on PC 2 (17.2%) (Figure 14; Table 9). Various aspects of spine orientation and infraspinous fossa shape seem to separate *Pongo* and *Homo* from the other taxa, while certain traits such as supraspinous length, total scapular length, and the ratio of the dorsal scapular fossae breadths contributed to the positive position of *Hylobates* along this axis. Similarly, the latter ratio, along with various superoinferior breadth characteristics, contributed to the positive position

TABLE 6. VARIABLE LOADINGS FOR THE 11-VARIABLE PRINCIPAL COMPONENTS ANALYSIS.

	PC1	PC2	
Infraspinous breadth/length	-0.970	-0.750	Axillary/infraspinous medial border angle
Axillary border/spine angle	-0.952	-0.582	Infraspinous neck/glenoid
Infraspinous breadth/glenoid	-0.920	-0.313	Ventral bar/glenoid angle
Ventral bar/glenoid angle	-0.723	-0.212	Axillary border/spine angle
Infraspinous neck/glenoid	0.448	-0.170	Infraspinous breadth/length
Axillary/infraspinous medial border angle	0.515	-0.138	Lateral expansion breadth/glenoid
Spine/glenoid angle	0.693	-0.068	Total length/glenoid
Infraspinous length/glenoid	0.768	-0.050	Supraspinous length/glenoid
Lateral expansion breadth/glenoid	0.795	-0.049	Spine/glenoid angle
Total length/glenoid	0.960	0.043	Infraspinous breadth/glenoid
Supraspinous length/glenoid	0.965	0.455	Infraspinous length/glenoid

TABLE 7. VARIABLE LOADINGS FOR THE 18-VARIABLE CANONICAL VARIATES ANALYSIS.

	CV1	CV2	
Axillary border/spine angle	-0.744	-0.292	Total length/glenoid
Infraspinous breadth/length	-0.724	-0.269	Supraspinous length/glenoid
Infraspinous breadth/glenoid	-0.468	-0.191	Axillary/medial border angle
Total breadth/length	-0.419	-0.191	Infraspinous neck/glenoid
Ventral bar/glenoid angle	-0.354	-0.161	Supraspinous/infraspinous breadth
Axillary/medial border angle	-0.194	-0.153	Axillary/infraspinous medial border angle
Infraspinous neck/glenoid	0.080	-0.129	Lateral expansion breadth/glenoid
Total breadth/glenoid	0.085	-0.092	Infraspinous length/glenoid
Axillary/infraspinous medial border angle	0.121	-0.061	Medial border/spine angle
Spine/glenoid angle	0.204	-0.039	Spine/glenoid angle
Supraspinous breadth/length	0.273	0.086	Ventral bar/glenoid angle
Lateral expansion breadth/glenoid	0.277	0.143	Supraspinous breadth/glenoid
Infraspinous length/glenoid	0.335	0.200	Axillary border/spine angle
Supraspinous/infraspinous breadth	0.456	0.235	Infraspinous breadth/glenoid
Total length/glenoid	0.510	0.257	Infraspinous breadth/length
Supraspinous length/glenoid	0.546	0.361	Total breadth/glenoid
Supraspinous breadth/glenoid	0.560	0.517	Total breadth/length
Medial border/spine angle	0.760	0.721	Supraspinous breadth/length

TABLE 8. VARIABLE LOADINGS FOR THE 11-VARIABLE CANONICAL VARIATES ANALYSIS.

	CV1	CV2	
Axillary border/spine angle	-0.851	-0.580	Axillary/infraspinous medial border angle
Infraspinous breadth/length	-0.833	-0.492	Total length/glenoid
Infraspinous breadth/glenoid	-0.544	-0.473	Supraspinous length/glenoid
Ventral bar/glenoid angle	-0.408	-0.435	Infraspinous neck/glenoid
Infraspinous neck/glenoid	0.101	-0.156	Lateral expansion breadth/glenoid
Axillary/infraspinous medial border angle	0.139	-0.120	Spine/glenoid angle
Spine/glenoid angle	0.225	-0.047	Ventral bar/glenoid angle
Lateral expansion breadth/glenoid	0.319	0.008	Axillary border/spine angle
Infraspinous length/glenoid	0.382	0.099	Infraspinous length/glenoid
Total length/glenoid	0.588	0.139	Infraspinous breadth/length
Supraspinous length/glenoid	0.624	0.284	Infraspinous breadth/glenoid

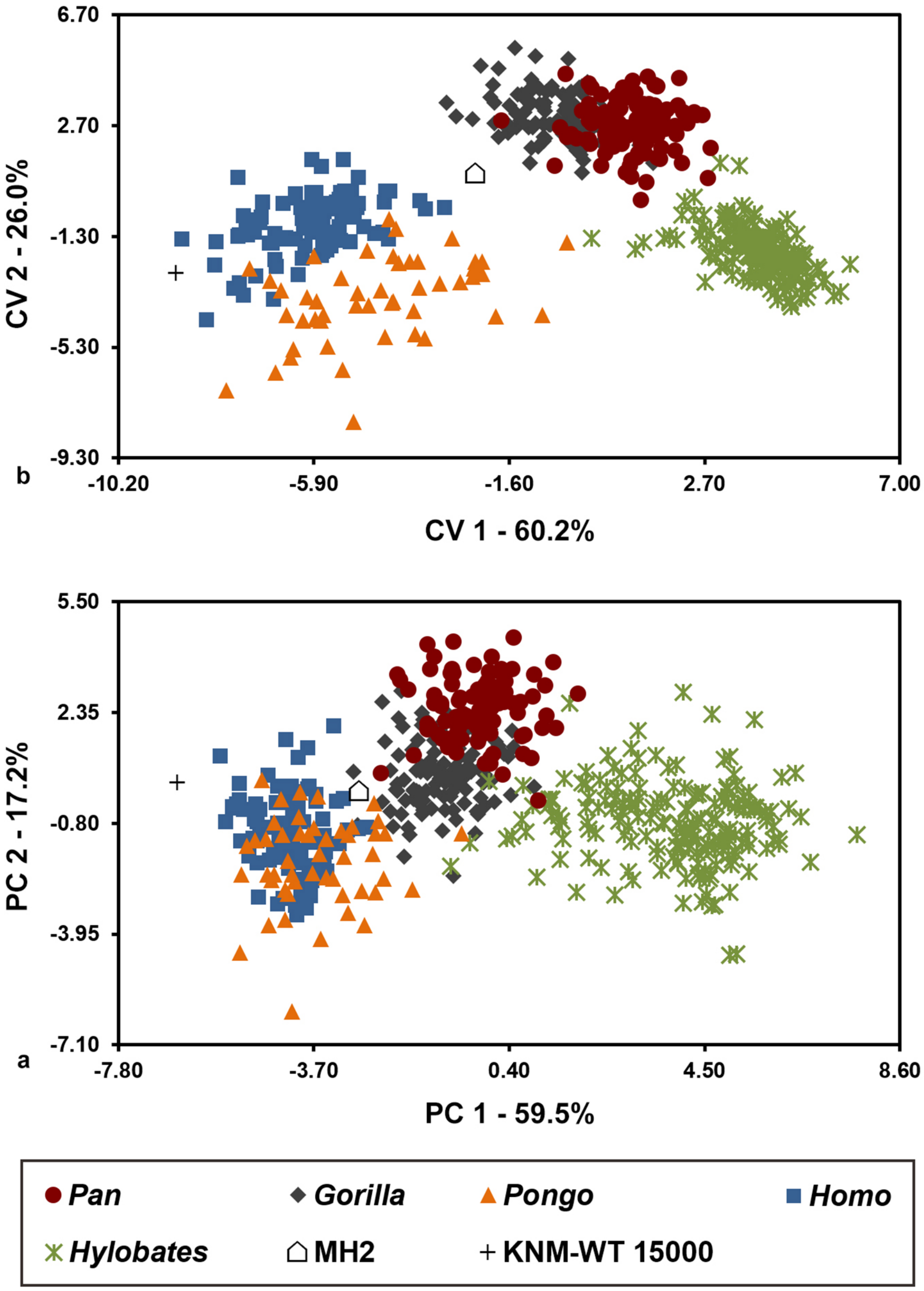

Figure 14. Plots depicting the first two axes for a) principal components and b) canonical variates analyses considering the 18 variables listed in Tables 5 and 7. There was a clear separation between the Homo *and* Pongo *data relative to* Hylobates *along PC 1;* Pan *and* Gorilla *were similar for PC 1, but separated along PC 2. Separation among the taxa was similar for the CVA, but with* Homo *and* Pongo *separating more along CV 2, and* Pan *and* Gorilla *separating along CV 1. In both instances, MH2 fell on the African ape "side" of the* Homo/Pongo *cluster, while KNM-WT 15000 fell on the opposite extreme.*

of the African apes in shape space, especially *Pan* (see Table 5). Extant *Homo* and *Pongo* clustered quite closely together, with some separation along PC 2. Both fossil specimens fell close to *Pongo* and *Homo* specimens along PC 1 and PC 2. MH2 fell at the upper end of the *Homo*/*Pongo* distribution where these individuals overlapped with the African apes along PC 1. KNM-WT 15000, on the other hand, displayed an extreme morphology with the most negative PC 1 value of all individuals (Figure 15; see Table 9).

By and large, many of the same variables driving the separation of the taxa in the PCA have similar loads in the CVA (see Table 7). As such, the overall pattern revealed by the CVA is similar to the PCA, although the African apes are more clearly separated from all groups, particularly along the second root axis (26%), and shifted more closely to *Hylobates* along the first root axis (60.2%) (see Figure 14; see Table 9). Separation between *Pongo* and modern humans is greater than in the PCA, and the Mahalanobis distance be-

TABLE 9. MEAN PC OR CV SCORE (and 95% confidence interval)
FOR EACH TAXON OR FOSSIL FOR THE 18-VARIABLE ANALYSES.

	PC1 (59.5%)	PC2 (17.2%)	CV1 (60.2%)	CV2 (26.0%)
Pan troglodytes	-0.25 (-0.42-0.09)^{a}	2.49 (2.30-2.67)^{a}	1.07 (0.90-1.24)^{a}	2.66 (2.47-2.86)^{a}
Gorilla gorilla	-0.99 (-1.13-0.85)^{b}	0.71 (0.52-0.90)^{b}	-0.53 (-0.69-0.37)^{b}	3.00 (2.84-3.17)^{a}
Homo sapiens	-4.24 (-4.37-4.10)^{c}	-0.99 (-1.23-0.75)^{c}	-6.00 (-6.24-5.76)^{c}	-0.88 (-1.11-0.65)^{b}
Pongo pygmaeus	-3.64 (-3.93-3.35)^{d}	-1.89 (-2.25-1.52)^{d}	-4.44 (-4.93-3.95)^{d}	-3.54 (-3.98-3.11)^{c}
Hylobates	3.81 (3.58-4.03)^{e}	-0.76 (-0.93-0.59)^{c}	3.90 (3.77-4.02)^{e}	-1.90 (-2.02-1.76)^{d}
MH2	-2.77	0.13	-2.36	0.95
KNM-WT 15000	-6.58	0.36	-8.94	-2.60

Differences between extant taxa were assessed by one-way ANOVA. Significant differences between adults were assessed using a post-hoc Tukey honestly significant difference test for multiple comparisons. Extant values with different superscript letters represent taxa that were significantly different at $\alpha \leq 0.05$ level; taxa with the same superscript were not significantly different.

tween them is significantly different (as was the case for all pairwise taxonomic comparisons) (Table 10). MH2 is closer to the grand mean of PC 1, near the upper limit of *Pongo* and outside of the extant *Homo* range, while KNM-WT 15000 falls at the negative end of the PC 1 axis. Along PC 2, however, KNM-WT 15000 is within the overlap regions of the modern human and *Pongo* data, while MH2 was at the upper bound of extant *Homo* (see Figure 15; see Table 9). All told, MH2 occupies a unique shape space between modern humans and the African apes.

For the 11-variable analyses, general separation between *Hylobates* and modern humans is maintained along the PC 1 axis (65.8%), although the taxa are more tightly clustered than in the broader analysis (Table 11). Notably,

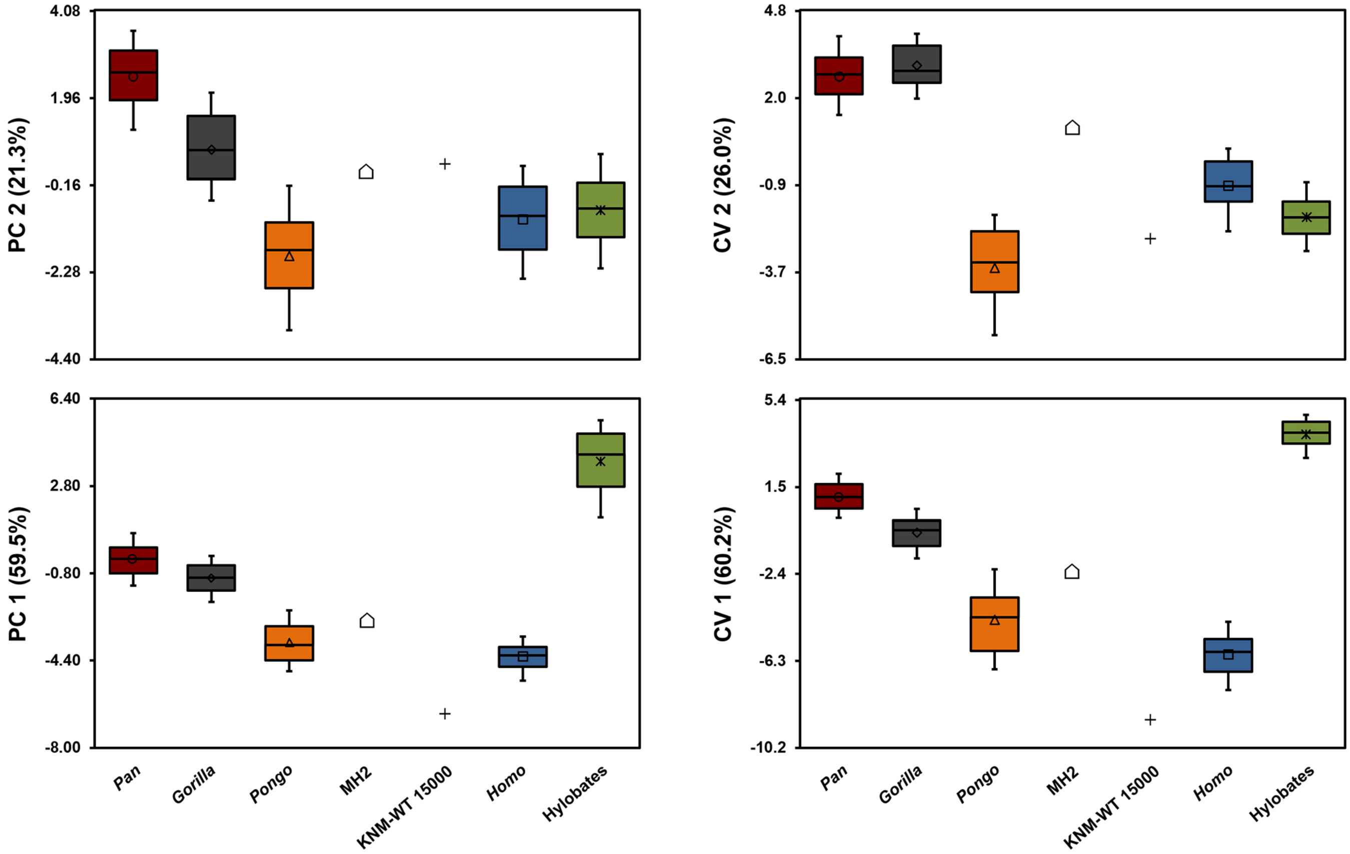

Figure 15. Box and whisker plots of the first two axes from the 18-variable principal components (left) and canonical variates (right) analyses depicted in Figure 14. Boxes encompass the middle 50% of the data range, while the central line represents the median value, and the whiskers extend from the lower 10% to the upper 90% of samples.

TABLE 10. MAHALANOBIS DISTANCES AND P-VALUES FOR THE 18-VARIABLE CVA.

	Homo	*Pan*	*Gorilla*	*Pongo*	*Hylobates*	MH2	KNM-WT 15000
Homo		**74.4**	**49.3**	**31.1**	**100.3**	**40.5**	**74.1**
Pan	**<0.001**		**17.0**	**74.7**	**36.7**	**46.7**	**214.8**
Gorilla	**<0.001**	**<0.001**		**72.4**	**45.2**	**43.2**	**173.3**
Pongo	**<0.001**	**<0.001**	**<0.001**		**85.0**	**74.9**	**126.6**
Hylobates	**<0.001**	**<0.001**	**<0.001**	**<0.001**		**74.7**	**232.7**
MH2							**126.6**
KNM-WT 15000							

Values above the diagonal are Mahalanobis distances; values below the diagonal are p-values for respective pairwise comparisons. All differences significant at $\alpha \leq 0.05$ are indicated in bold. *Pan* individuals were correctly classified 92.6% of the time (seven were misclassified as *Gorilla*); *Pongo* was correctly classified at a rate of 93.9% (two were misclassified as *Homo*, one was misclassified as *Hylobates*); *Hylobates* was 99.4% correct (one individual was misclassified as *Pan*).

there is a greater separation of *Pongo* and modern humans, particularly along PC 2 (11.9%) (Figures 16 and 17). This is likely driven by differences in AIM angle, infraspinous neck size, and VBG angle (see Table 6). Additionally, there is more overlap between extant *Homo* and *Gorilla*, and seemingly greater division between the latter and *Pan*. Fossil hominins are all positioned close to the distribution of extant *Homo* specimens on PC 1, though KNM-WT 15000 and MH2 fall at opposite sides of the modern human sample on this PC axis (see Figure 16). KSD-VP-1/1 falls near the middle of the *Homo* data for PC 1, but had a more positive PC 2 score, such that it fell among the *Pongo* data scatter; both KNM-WT 15000 and MH2 fell among the modern *Homo* data for PC 2 (see Table 11).

The 11-variable CVA exhibits similar results to the PCA, but with greater separation between modern humans and *Pongo*/*Gorilla* (see Table 8). Despite some taxonomic "misclassifications," all Mahalanobis distances between extant taxa are significantly different (Table 12). Both MH2 and KSD-VP-1/1 fall among the *Pongo* distribution, and

TABLE 11. MEAN PC OR CV SCORE (and 95% confidence interval)
FOR EACH TAXON OR FOSSIL FOR THE 11-VARIABLE ANALYSES.

	PC1 (65.8%)	**PC2 (11.9%)**	**CV1 (76.0%)**	**CV2 (17.4%)**
Pan troglodytes	-0.55 (-0.68-0.41)^{a}	1.60 (1.45-1.76)^{a}	0.57 (0.38-0.75)^{a}	2.97 (2.76-3.17)^{a}
Gorilla gorilla	-1.00 (-1.12-0.87)^{b}	-0.38 (-0.50-0.26)^{b}	-1.05 (-1.24-0.86)^{b}	0.03 (-0.11-0.18)^{b}
Homo sapiens	-3.30 (-3.44-3.16)^{c}	-1.10 (-1.22-0.98)^{c}	-5.38 (-5.61-5.14)^{c}	-1.44 (-1.63-1.24)^{c}
Pongo pygmaeus	-2.58 (-2.83-2.33)^{d}	0.46 (0.25-0.67)^{d}	-2.66 (-3.03-2.29)^{d}	0.83 (0.53-1.12)^{d}
Hylobates	3.24 (3.06-3.43)^{e}	-0.19 (-0.33-0.05)^{b}	3.72 (3.59-3.86)^{e}	-1.09 (-1.26-0.92)^{c}
MH2	-2.27	-0.88	-3.23	0.52
KNM-WT 15000	-5.44	-1.07	-7.95	-4.27
KSD-VP-1-1	-3.66	1.16	-3.08	2.03

Differences between extant taxa was assessed by one-way ANOVA. Significant differences between adults were assessed using a post-hoc Tukey honestly significant difference test for multiple comparisons. Extant values with different superscript letters represent taxa that were significantly different at $\alpha \leq 0.05$ level; taxa with the same superscript were not significantly different.

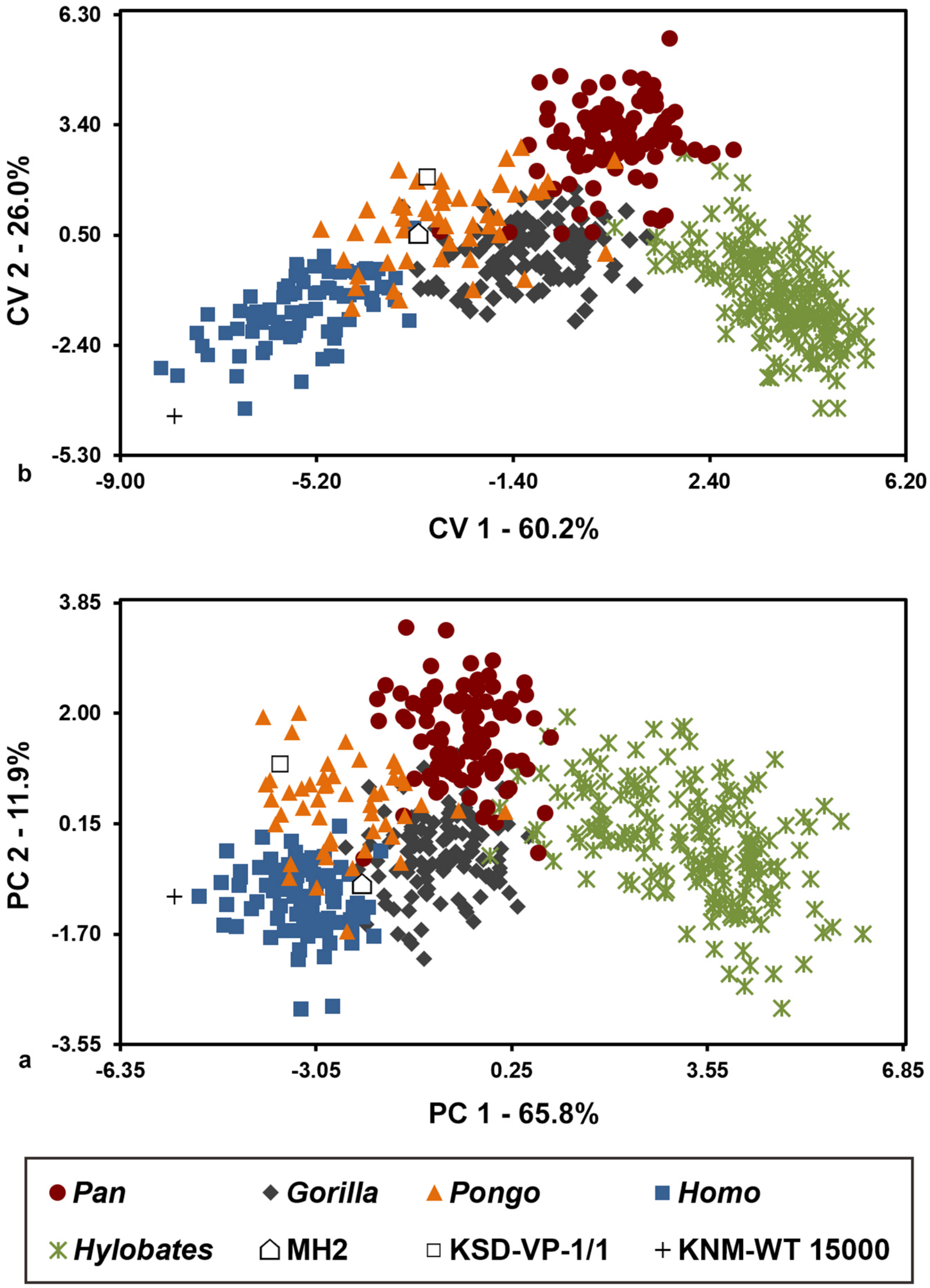

Figure 16. Plots depicting the first two axes for a) principal components and b) canonical variates analyses considering the 11 variables listed in Tables 6 and 8. Overall results were similar to the 18-variable analysis, although there was greater separation between Pongo *and* Homo, *and between* Pan *and* Gorilla, *positively along PC 2. MH2 and KNM-WT 15000 occupied similar ends of the* Homo *data cluster as before, which positioned MH2 near the* Homo/Pongo/Gorilla *overlap in morphospace. In both analyses, KSD-VP-1/1 fell among* Pongo *data.*

were notably distinct from modern humans. KNM-WT 15000 plots at the extreme negative end of both PC axes, as has been the case with the previous analyses. Unsurprisingly, the multivariate analysis based on the larger dataset appears to have done a better job of separating the taxa and fossil individuals, as judged by the Mahalanobis distance scores and posterior probabilities (see Table 12).

Humeral Morphology

While the fragmentary nature of most early hominin humeri makes functional interpretation of their morphology difficult, the humeral heads of the australopiths are said to be elliptical with an intertubercular, or bicipital, groove that is relatively shallow and with projecting lesser tubercles—unlike African apes with their spherical humeral heads, deep bicipital grooves, and less projecting tubercles (Larson 2013). In some respects, the australopith pattern is

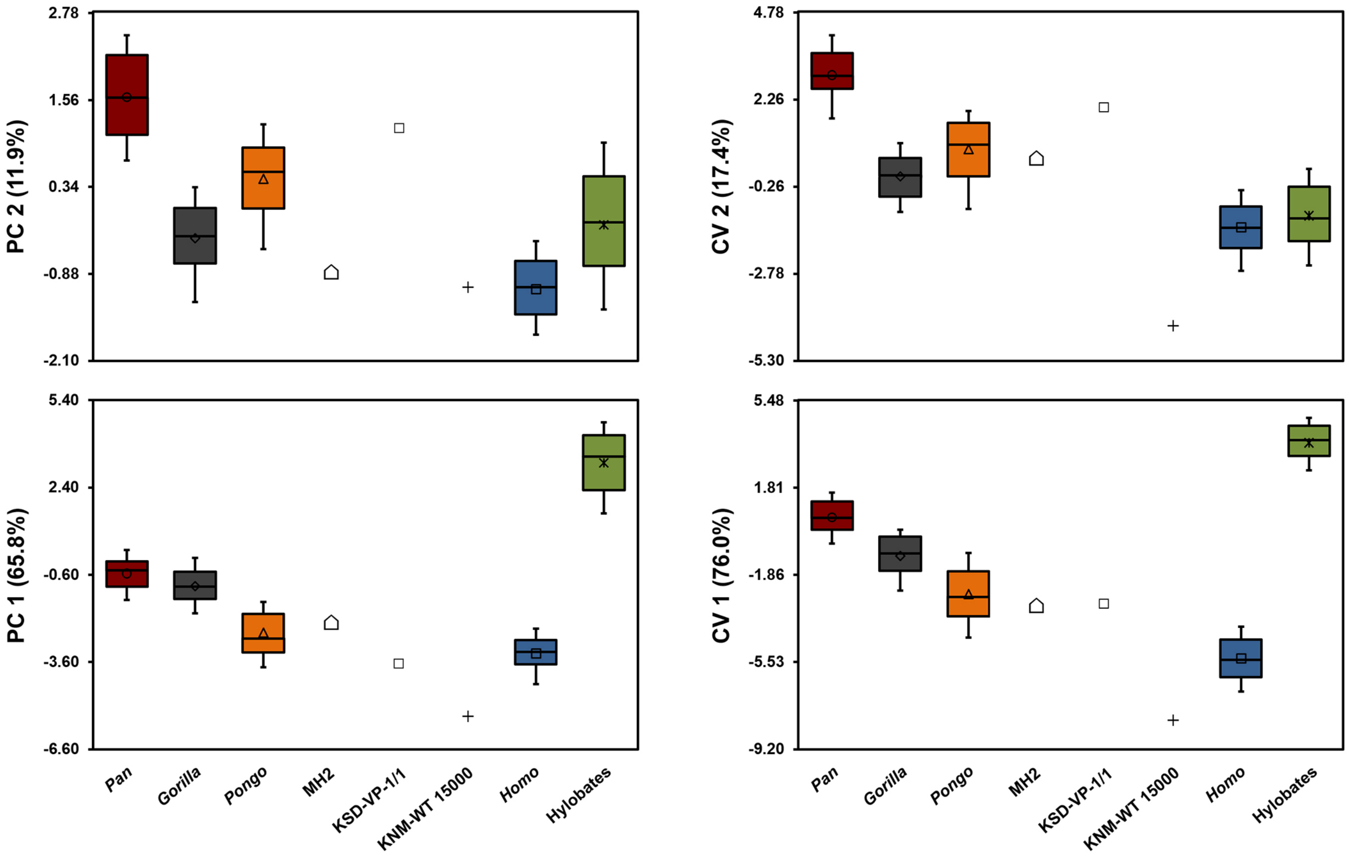

Figure 17. Box and whisker plots of the first two axes from the 11-variable principal components (left) and canonical variates (right) analyses depicted in Figure 16. Boxes encompass the middle 50% of the data range, while the central line represents the median value, and the whiskers extend from the lower 10% to the upper 90% of samples.

manifested in *Au. sediba*—the humeral heads of MH2 are both elliptical in dorsal view with lesser tubercles that project more than is typical of modern humans and extant apes. This is similar to *Au. africanus* (Sts 7: Broom et al. 1950) and *Au. afarensis* (KNM-BC 1745: Pickford et al. 1983; A.L. 288-1: Johanson et al. 1982). Notably, however, proximal humeri in *Au. sediba* differ in having bicipital grooves that are narrow and deep, which is more similar to African apes and *H. naledi* (Berger et al. 2015; Feuerriegel et al. 2017).

As most known early fossil humeri are incomplete or damaged, accurate measurement of humeral torsion has presented a significant obstacle in evolutionary studies. Larson (1996) devised two methodologies for estimating degree of humeral torsion on incomplete fossil humeri using sets of alternative reference axes and multiple regression analyses, producing estimated torsion measurements of 124° for AL 288-1, 126° for Sts 7, and 130° for Omo 119-73-2718 (attributed to *Au.* cf. *africanus*: Howell and Coppens 1976), and 111° for KNM-ER 739 (attributed to *Au.* cf. *boisei*: Howell and Coppens 1976; Lague 2015). Early Pleistocene hominin humeri appear to be characterized by low to modest amounts of humeral torsion, suggesting that low humeral torsion is the primitive condition for fossil hominins (Larson 2007). This interpretation is further reinforced by torsion measurements from *Au. sediba*—MH2 has an estimated humeral torsion value of 117°, while the MH1 juvenile specimen has a value of 112° (Churchill et al. 2013).

The humeral medial epicondyle is strongly projecting in the Malapa hominins, such that the ratio of humeral distal articular breadth to biepicondylar breadth is smaller in them (mean ratio of 0.643±0.026) compared to a sample of australopiths (0.677±0.044, n=11) and modern humans (0.665±0.041, n=100) (Churchill et al. 2013). The medial epicondyle in MH2 is less retroflexed and more distally oriented than that of A.L. 288-1, resulting in reduced torque for pronation of the forearm relative to A.L. 288-1 (Ibáñez-Gimeno et al. 2017). As with other australopiths, the humeral lateral epicondyle is pronounced and exhibits an elongated brachioradialis crest. In terms of humeral distal articular shape, the Malapa hominins are similar to African apes (and not modern humans) in having trochleae with subequal PD and ML dimensions, and trochleae that are ML broad relative to the capitulum (Macias 2015).

Radial And Ulnar Morphology

Most early hominins exhibit proximal ulnar morphology resembling that of modern humans, albeit somewhat intermediate between that of modern humans and chimpanzees (see Drapeau 2004; Drapeau et al. 2005). Drapeau (2004; Drapeau et al. 2005) quantified olecranon process

TABLE 12. MAHALANOBIS DISTANCES AND P-VALUES FOR THE 11-VARIABLE CVA.

	Homo	*Pan*	*Gorilla*	*Pongo*	*Hylobates*	MH2	KNM-WT 15000	KSD-VP-1/1
Homo		**54.8**	**24.2**	**17.1**	**83.2**	**20.8**	**62.7**	**36.3**
Pan	**<0.001**		**13.9**	**19.5**	**26.7**	**32.1**	**170.8**	**31.6**
Gorilla	**<0.001**	**<0.001**		**9.49**	**26.2**	14.7	**115.4**	**20.8**
Pongo	**<0.001**	**<0.001**	**<0.001**		**47.3**	**22.5**	**104.8**	**26.7**
Hylobates	**<0.001**	**<0.001**	**<0.001**	**<0.001**		**63.5**	**192.9**	**73.4**
MH2							**100.5**	20.8
KNM-WT 15000								**98.7**
KSD-VP-1/1								

Values above the diagonal are Mahalanobis distances; values below the diagonal are p-values for respective pairwise comparisons. All differences significant at $\alpha \leq 0.05$ are indicated in bold. *Homo* individuals were correctly classified 96.5% of the time (two were misclassified as *Gorilla* and one was misclassified as *Pongo*); *Pan* individuals were correctly classified 92.6% of the time (seven were misclassified as *Gorilla*); *Pongo* was correctly classified at a rate of only 73.5% (four were misclassified as *Homo*, two were misclassified as *Pan*, and seven were misclassified as *Gorilla*); *Hylobates* was 96.1% correct (three were was misclassified as *Pan* and four were misclassified as *Gorilla*).

orientation in four fossil hominin ulnae—A.L. 438-1 and A.L. 288-1 (*Au. afarensis*; Drapeau et al. 2005; Johanson et al. 1982), L40-19 (a robust australopith of uncertain taxonomy: Howell and Coppens 1976; McHenry et al. 1976), and OH 36 (which has been attributed to both *Au. (P.) boisei* [Aiello et al. 1999; Walker and Leakey 1993] and *H. erectus* [Day 1978, 1986; Leakey 1978]). *Ardipithecus ramidus* appears to have maintained a retroflexed olecranon much like great apes (Lovejoy et al. 2009), while other early hominins have a more proximally oriented *M. triceps brachii* lever arm (Drapeau 2004; Drapeau et al. 2005), falling outside the sample ranges for apes either near the modern human mean (L40-19) or at the high end of the ape sample ranges (A.L. 438-1, A.L. 288-1, and OH 36). Olecranon orientation in MH2 (taken on the reconstructed ulna, following Drapeau [2004]) is 120°, falling between A.L. 288-1 and OH 36 (see Figure 5 in Drapeau 2004) and well above the modern human and most ape sample means. *Au. sediba* also falls within observed ranges reported for other australopiths and early *Homo* in measures of the mechanical advantage of *M. triceps brachii* (calculated as olecranon process length divided by the articular length of the ulna, the latter taken as the distance from the proximodistal midpoint of trochlear notch to the distal-most articular surface of the head) (Churchill et al. 2013). Similarity in olecranon morphology between specimens of *Au. afarensis* and *Au. sediba* suggests that a proximally orientated olecranon may be the primitive condition for *Australopithecus*. This morphology derives its advantage in providing greater mechanical leverage to the *M. triceps brachii* during 90° arm flexion, maximizing force generation produced by a flexed forearm. Given that it appears unlikely that quadrupedalism involving forearm flexion was a significant selective pressure in *Australopithecus* species (Ward 2013), it is probable that the proximally oriented olecranon of early fossil hominins, including *Au. sediba*, arose through directional selection for manipulatory behaviors, if not necessarily tool manufacture.

The proximal articulation of the ulna in MH2 is small relative to the overall size of the bone (Rein et al. 2017) compared to ulnae of *Au. afarensis* and African apes, a feature which has been interpreted as indicating a significant component of forelimb suspension in the locomotor repertoire of *Au. sediba* (Rein et al. 2017). The trochlear surfaces of both the MH1 and MH2 ulnae exhibit moderate keeling, which may also signify habitual climbing and suspension by *Au. sediba* (see Drapeau 2008). Interestingly, the anteriorly opening orientation of the trochlear notch in the specimens from Malapa is more like that of specimens of *Au. afarensis* (A.L. 288-1, A.L. 438-1, and KSD-VP-1/1: Drapeau et al. 2005; Haile-Selassie et al. 2010; Johanson et al. 1982) and the *Homo erectus* specimen KNM-WT 15000 (SEC personal observation) than it is like geographically proximal specimens of *Au. africanus* (StW 113, StW 398, and probably StW 380 and StW 431: SEC personal observation), which open anteroproximally. Anteriorly oriented trochlear notches have been argued to reflect maximal cubital loading with the forearm in flexed rather than extended positions (Trinkaus 1989), which may indicate important variation in upper limb use within the genus *Australopithecus*. Although the orientation of the trochlear notch may suggest peak elbow loading with a flexed forearm, the primary muscles that produce flexion (*Mm. brachialis* and *biceps brachii*) do not appear to have had great mechanical advantage in *Au. sediba*. The mechanical advantage of *M. brachialis* (taken as ulnar tuberosity position/ulnar articular length) in MH2 (0.127) is below that of other australopiths (0.145±0.009, n=3) and modern humans (0.156±0.011, n=30), while the length of the radial neck relative to radial head size (as a measure of the relative length of the *M. biceps brachii* moment arm) is also small in MH2 (1.49) compared to other australopiths (1.84±0.25, n=3) and modern humans (1.53±0.10, n=30) (Churchill et al. 2013). However, MH2 exhibits a radial tuberosity that is long relative to radial head size (1.51) compared to other australopiths (1.27±0.24, n=5) and modern humans (1.05±0.10, n=30) (Churchill et al. 2013), which may indicate greater hypertrophy of the forearm flexors to compensate for their reduced mechanical advantage.

The radial shaft of MH2 is mildly curved in anterior perspective, and exhibits a medialward inflection of its distal third. This inflection results in a medial inclination of the distal carpal articular surface, which is consistent with a more distally oriented scapholunate articulation and attendant distomedial rotation of the scaphoid (Kivell et al. 2018), although the functional significance of this feature is uncertain. The distal radii of both MH1 and MH2 share with other australopiths in having larger lunate than scaphoid articular facets and weakly developed but distinct dorsal ridges on their radiocarpal articular margins (see Kimbel and Delezene 2009).

Summary

Although *Au. sediba* shares a number of derived features with fossil and extant *Homo* in its craniodental (Berger et al. 2010; de Ruiter et al. 2013), manual (Kivell et al. 2011), pelvic (Kibii et al. 2011), and pedal (Zipfel et al. 2011) morphology, its pectoral, arm, and forearm morphology appears to be largely primitive. *Australopithecus sediba* is African apelike in its clavicular length proportions, curvatures, and orientation, and in its scapular ventral bar/glenoid angle and scapular spine orientation. In terms of its position in multivariate shape space, the MH2 scapula falls within or close to *Pongo*/modern human combined data scatters, within *Pongo*, or between modern human and African ape data scatters. Taken together, these characteristics denote a scapula that was positioned high on the thorax as in apes, and imply an upper limb that was habitually used in overhead arm postures in the context of arboreal locomotion and positional behaviors.

Australopithecus sediba is also similar to other australopiths in having an elliptical humeral head (in dorsal perspective) with projecting lesser tubercles, positioned on a humerus with a low amount of torsion to the diaphysis (such that the humeral head is directed posteriorly). The morphology of the distal humerus and proximal radius and ulna is generally like that of other australopiths, although the proximal ulnar articulation in MH2 is small relative to the overall size of the bone compared to A.L. 288-1, possibly reflecting greater forelimb suspensory behaviour in the former (Rein et al. 2017). Other aspects of the forearms of the Malapa hominins also suggest a retained adaptation for arboreal locomotion in *Au. sediba*, perhaps more so than found in *Au. afarensis*. These features include a square-shaped ulnar trochlear notch (Rein et al. 2017), ulnar trochlear keeling (Churchill et al. 2013), robust origination and insertion sites for wrist and finger flexors such as *M. flexor carpi ulnaris* (Berger et al. 2010; Kivell et al. 2011), and moderate yet distinct phalangeal curvature (Kivell et al. 2011). The overall picture that emerges from the well-preserved upper limbs of *Au. sediba* is a pectoral gridle and forelimb (excluding the wrist and hand) that was predominantly primitive in its morphology, suggesting the retention of substantial climbing and suspensory ability in the Malapa hominins.

ACKNOWLEDGEMENTS

We thank the South African Heritage Resource agency for the permits to work at the Malapa site; the Nash family for granting access to the Malapa site and continued support of research on their reserve; the South African Department of Science and Technology, the South African National Research Foundation, the Institute for Human Evolution, University of the Witwatersrand, the Palaeontological Scientific Trust, the Andrew W. Mellon Foundation, the U.S. Diplomatic Mission to South Africa, the A.H. Schultz Foundation, the National Geographic Society, and Sir Richard Branson for funding; the University of the Witwatersrand's Schools of Geosciences and Anatomical Sciences and the Bernard Price Institute for Palaeontology for support and facilities; the Gauteng Government, Gauteng Department of Agriculture, Conservation and Environment, and the Cradle of Humankind Management Authority. For access to comparative specimens, E. Mbua, P. Kiura, V. Iminjili, and the National Museums of Kenya, B. Billings, B. Zipfel, and the School of Anatomical Sciences at the University of the Witwatersrand, and S. Potze, L.C. Kgasi, and the Ditsong Museum. For technical and material support, Optech and Optron; Duke University; and, the University of Zurich 2009 and 2010 Field Schools. Numerous individuals were involved in the ongoing preparation and excavation of these fossils, including C. Dube, C. Kemp, M. Kgasi, M. Languza, J. Malaza, G. Mokoma, P. Mukanela, T. Nemvhundi, M. Ngcamphalala, S. Jirah, S. Tshabalala, and C. Yates. Other individuals who have given significant support to this project include B. de Klerk, C. Steininger, B. Kuhn, L. Pollarolo, B. Zipfel, J. Kretzen, D. Conforti, J. McCaffery, C. Dlamini, H. Visser, R. McCrae-Samuel, B. Nkosi, B. Louw, L. Backwell, F. Thackeray, and M. Peltier. J. Smilg facilitated computed tomography scanning of the

specimens. To all of these individuals and organizations we are grateful.

ENDNOTES

1. It has been suggested that differences in the ranges of variation in VBG in human ontogenetic samples reported by Inouye and Shea (1997: in which they observed values to 120° and an outlier at ca. 108°) and Green and Alemseged (2012: in which the lowest observed value was 139.6°) further calls into question the validity of this angle as a measure of glenoid fossa orientation. However, similarity of sample means and measures of dispersion in the two studies (141.0±7.6° vs. 142.4±5.5°, respectively) argues against undue interobserver error, and supports the use of this angle as a measure of scapular shape.

REFERENCES

Aiello, L.C., Wood, B., Key, C., and Lewis, M. 1999. Morphological and taxonomic affinities of the Olduvai ulna (OH 36). *American Journal of Physical Anthropology* 109, 89–110.

Alemseged, Z., Spoor, F., Kimbel, W.H., Bobe, R., Geraads, D., Reed, D., and Wynn, J.G. 2006. A juvenile early hominin skeleton from Dikika, Ethiopia. *Nature* 443, 296–301.

Berger, L.R., de Ruiter, D.J., Churchill, S.E., Schmid, P., Carlson, K.J., Dirks, P.H.G.M., and Kibii, J.M. 2010. *Australopithecus sediba*: a new species of *Homo*-like australopith from South Africa. *Science* 328, 195–204.

Berger, L.R., Hawks, J., de Ruiter, D.J., Churchill, S.E., Schmid, P., Delezene, L.K., Kivell, T.L., Garvin, H.M., Williams, S.A., DeSilva, J.M., Skinner, M.M., Musiba, C.M., Cameron, N., Holliday, T.W., Harcourt-Smith, W., Ackermann, R.R., Bastir, M., Bogin, B., Bolter, D., Brophy, J., Cofran, Z.D., Congdon, K.A., Deane, A.S., Dembo, M., Drapeau, M., Elliott, M.C., Feuerriegel, E.M., Garcia-Martinez, D., Green, D.J., Gurtov, A., Irish, J.D., Kruger, A., Laird, M.F., Marchi, D., Meyer, M.R., Nalla, S., Negash, E.W., Orr, C.M., Radovcic, D., Schroeder, L., Scott, J.E., Throckmorton, Z., Tocheri, M.W., VanSickle, C., Walker, C.S., Wei, P., and Zipfel, B. 2015. *Homo naledi*, a new species of the genus *Homo* from the Dinaledi Chamber, South Africa. *eLife* 4, e09560.

Broom, R., Robinson, J.T., and Schepers, G.W.H. 1950. Sterkfontein Ape-Men *Plesianthropus*. *Transvaal Museum Memoir* 4, 1–104.

Carretero, J.M., Arsuaga, J.L., and Lorenzo, C. 1997. Clavicles, scapulae and humeri from the Sima de los Huesos site (Sierra de Atapuerca, Spain). *Journal of Human Evolution* 33, 357–408.

Churchill, S.E., 1994. *Human Upper Body Evolution in the Eurasian Later Pleistocene*. Ph.D. Dissertation, University of New Mexico.

Churchill, S.E., Holliday, T.W., Carlson, K.J., Jashashvili, T., Macias, M.E., Mathews, S., Sparling, T.L., Schmid, P., de Ruiter, D.J., and Berger, L.R. 2013. The upper limb of *Australopithecus sediba. Science* 340, 1233477.

Churchill, S.E. and Trinkaus, E. 1990. Neandertal scapular glenoid morphology. *American Journal of Physical Anthropology* 83, 147–160.

Day, M.H. 1978. Hominid postcranial material from Bed I, Olduvai Gorge. In: Isaac, G.L. and McCowan, E.R. (eds.), *Human Origins: Louis Leakey and the East African evidence.* W.A. Benjamin, Menlo Park, CA, pp. 363–374.

Day, M.H., 1986. *Guide to Fossil Man*, 4th Edition. University of Chicago Press, Chicago.

de Ruiter, D.J., DeWitt, T.J., Carlson, K.B., Brophy, J.K., Schroeder, L., Ackermann, R.R., Churchill, S.E., and Berger, L.R. 2013. Mandibular remains support taxonomic validity of *Australopithecus sediba*. *Science* 340, e1232997.

Drapeau, M.S.M. 2004. Functional anatomy of the olecranon process in hominoids and Plio-Pleistocene hominins. *American Journal of Physical Anthropology* 124, 297–314.

Drapeau, M.S.M. 2008. Articular morphology of the proximal ulna in extant and fossil hominoids and hominins. *Journal of Human Evolution* 55, 86–102.

Drapeau, M.S.M., Ward, C.V., Kimbel, W.H., Johanson, D.C., and Rak, Y. 2005. Associated cranial and forelimb remains attributed to *Australopithecus afarensis* from Hadar, Ethiopia. *Journal of Human Evolution* 48, 593–642.

Feuerriegel, E.M., Green, D.J., Walker, C.S., Schmid, P., Hawks, J., Berger, L.R., and Churchill, S.E. 2017. The upper limb of *Homo naledi*. *Journal of Human Evolution* 104, 155–173.

Green, D.J. 2013. Ontogeny of the hominoid shoulder: the influence of locomotion on morphology. *American Journal of Physical Anthropology* 152, 239–260.

Green, D.J. and Alemseged, Z. 2012. *Australopithecus afarensis* scapular ontogeny, function, and the role of climbing in human evolution. *Science* 338, 514–517.

Green, D.J., Chirchir, H., Mbua, E., Harris, J.W.K., Braun, D.R., Griffin, N.L., and Richmond, B.G. 2018. Scapular anatomy of *Paranthropus boisei* from Ileret, Kenya. *Journal of Human Evolution* 125, 181–192.

Haile-Selassie, Y., Latimer, B.M., Alene, M., Deino, A.L., Gibert, L., Melillo, S.M., Saylor, B.Z., Scott, G.R., and Lovejoy, C.O. 2010. An early *Australopithecus afarensis* postcranium from Woranso-Mille, Ethiopia. *Proceedings of the National Academy of Sciences USA* 107, 12121–12126.

Harrington, M.A., Keller, T.S., Seiler, J.G., Weikert, D.R., Moeljanto, E., and Schwartz, H.S. 1993. Geometric properties and the predicted mechanical behaviour of adult human clavicles. *Journal of Biomechanics* 26, 417–426.

Howell, F.C. and Coppens, Y. 1976. An overview of Hominidae from the Omo Succession, Ethiopia. In *Earliest Man and Environments in the Lake Rudolf Basin*, Coppens, Y., Howell, F.C., Isaac, G.L., and Leakey, R.E.F. (eds.). University of Chicago Press, Chicago, pp. 522–532.

Hunt, K.D. 1991. Mechanical implications of chimpanzee positional behavior. *American Journal of Physical Anthropology* 86, 521–536.

Ibáñez-Gimeno, P., Manyosa, J., Galtés, I., Jordana, X., Moyà-Solà, S., and Malgosa, A. 2017. Forearm pronation efficiency in A.L. 288-1 (*Australopithecus afarensis*) and MH2 (*Australopithecus sediba*): insights into their locomotor and manipulative habits. *American Journal of Physical Anthropology* 164, 788–800.

Ihaka, R. and Gentleman, R. 1996. R: a language for data analysis and graphics. *Journal of Computational and Graphical Statistics* 5, 299–314.

Inouye, S.E. and Shea, B.T. 1997. What's your angle? Size correction and bar-glenoid orientation in "Lucy" (A.L. 288-1). *International Journal of Primatology* 18, 629–650.

Johanson, D.C., Lovejoy, C.O., Kimbel, W.H., White, T.D., Ward, S.C., Bush, M.E., Latimer, B.M., and Coppens, Y. 1982. Morphology of the Pliocene partial hominid skeleton (A.L. 288-1) from the Hadar Formation, Ethiopia. *American Journal of Physical Anthropology* 57, 403–451.

Kibii, J.M., Churchill, S.E., Schmid, P., Carlson, K.J., Reed, N.D., de Ruiter, D.J., and Berger, L.R. 2011. A partial pelvis of *Australopithecus sediba. Science* 333, 1407–1411.

Kimbel, W.H. and Delezene, L.K. 2009. "Lucy" redux: A review of research on *Australopithecus afarensis*. *Yearbook of Physical Anthropology* 52, 2–48.

Kivell, T.L., Churchill, S.E., Kibii, J.M., Schmid, P., and Berger, L.R. 2018 (this volume). The hand of *Australopithecus sediba*. *PaleoAnthropology* 2018, 282–333.

Kivell, T.L., Kibii, J.M., Churchill, S.E., Schmid, P., and Berger, L.R. 2011. *Australopithecus sediba* hand demonstrates mosaic evolution of locomotor and manipulative abilities. *Science* 333, 1411–1417.

L'Abbé, E.N., Symes, S.A., Pokines, J.T., Cabo, L.L., Stull, K.E., Kuo, S., Raymond, D.E., Randolph-Quinney, P.S., and Berger, L.R. 2015. Evidence of fatal skeletal injuries on Malapa Hominins 1 and 2. *Scientific Reports* 5, e15120.

Lague, M.R. 2015. Taxonomic identification of Lower Pleistocene fossil hominins based on distal humeral diaphyseal cross-sectional shape. *PeerJ* 3, e1084

Larson, S.G. 1995. New characters for the functional interpretation of primate scapulae and proximal humeri. *American Journal of Physical Anthropology* 98, 13–35.

Larson, S.G. 1996. Estimating humeral torsion on incomplete fossil anthropoid humeri. *Journal of Human Evolution* 31, 239–257.

Larson, S.G. 2007. Evolutionary transformation of the hominin shoulder. *Evolutionary Anthropology* 16, 172–187.

Larson, S.G. 2013. Shoulder morphology in early hominin evolution. In *The Paleobiology of* Australopithecus, Reed, K.E., Fleagle, J.G., and Leakey, R.E.F. (eds.). Springer, Dordrecht, pp. 247–261.

Larson, S.G., Jungers, W.L., Tocheri, M.W., Orr, C.M., Morwood, M.J., Sutikna, T., Due Awe, R., and Djubiantono, T. 2009. Descriptions of the upper limb skeleton of *Homo floresiensis*. *Journal of Human Evolution* 57, 555–570.

Leakey, M.D. 1978. Olduvai fossil hominids: their stratigraphic positions and associations. In *Early Hominids of Africa*, Jolly, C.J. (ed.). Duckworth, London, pp. 3–16.

Lovejoy, C.O., Johanson, D.C., and Coppens, Y. 1982. Hominid upper limb bones recovered from the Hadar Formation: 1974–1977 collections. *American Journal of Physical Anthropology* 57, 637–649.

Lovejoy, C.O., Simpson, S.W., White, T.D., Asfaw, B., and Suwa, G. 2009. Careful climbing in the Miocene: the forelimbs of *Ardipithecus ramidus* and humans are primitive. *Science* 326, 70-70e8.

Macias, M.E. 2015. *Functional Integration of the Hominin Forelimb*. Ph.D. Dissertation, Duke University.

Martin, R. 1928. *Lehrbuch der Anthropologie*. Verlag von Gustav Fischer, Jena.

Mathews, S. 2017. *The Evolution of the Human Shoulder Girdle: Functional Morphology and Evolutionary Origin of its Pathologies*. Ph.D. Dissertation, University of Zurich.

Mathews, S., Frater, N., Bonneau, N., and Haeusler, M. 2016. Osteoarthritis and human evolution, Abstracts of the International Society for Evolution, Medicine & Public Health, Durham, NC. https://easychair.org/smart-program/ISEMPH2016/2016-06-24.html

Mays, S., Steele, J., and Ford, M. 1999. Directional asymmetry in the human clavicle. *International Journal of Osteoarchaeology* 9, 18–28.

McHenry, H.M., Corruccini, R.S., and Howell, F.C. 1976. Analysis of an early hominid ulna from the Omo Basin, Ethiopia. *American Journal of Physical Anthropology* 44, 295–304.

Melillo, S.M. 2011. *Anatomy of the* Australopithecus *Scapula and Evolution of the Human Shoulder: Insights from a New Fossil Specimen, KSD-VP-1/1G*. Ph.D. Dissertation, Stanford University.

Melillo, S.M. 2015. An alternative interpretation of the *Australopithecus* scapula. *Proceedings of the National Academy of Sciences USA* 112, E7159.

Melillo, S.M. 2016. The shoulder girdle of KSD-VP-1/1. In *The Postcranial Anatomy of* Australopithecus afarensis*: New Insights from KSD-VP-1/1*, Haile-Selassie, Y. and Su, D.F. (eds.). Springer, Dordrecht, pp. 113–141.

Ohman, J.C. 1986. The first rib of hominoids. *American Journal of Physical Anthropology* 70, 209–229.

Partridge, T.C., Granger, D.E., Caffee, M.W., and Clarke, R.J. 2003. Lower Pliocene hominid remains from Sterkfontein. *Science* 300, 607–612.

Pickford, M., Johanson, D.C., Lovejoy, C.O., White, T.D., and Aronson, J.L. 1983. A hominoid humeral fragment from the Pliocene of Kenya. *American Journal of Physical Anthropology* 60, 337–346.

Preuschoft, H., Hohn, B., Scherf, H., Schmidt, M., Krause, C., and Witzel, U. 2010. Functional analysis of the primate shoulder. *International Journal of Primatology* 31, 301–320.

Rein, T.R., Harrison, T., Carlson, K.J., and Harvati, K. 2017. Adaptation to suspensory locomotion in *Australopithecus sediba*. *Journal of Human Evolution* 104, 1–12.

Schuenke, M., Schulte, E., Schumacher, U., Ross, L.M., and Lamperti, E.D. 2007. *Thieme Atlas of Anatomy: General Anatomy and Musculoskeletal System*. Thieme Medical Publishers, New York.

Smith, R.J. and Jungers, W.L. 1997. Body mass in comparative primatology. *Journal of Human Evolution* 32, 523–559.

Solan, M. and Day, M.H. 1992. The Baringo (Kapthurin) ulna. *Journal of Human Evolution* 22, 307–313.

StatSoft, 2014. STATISTICA (data analysis software system).

Steele, D.G. 1970. Estimation of stature from fragments of long limb bones. In *Personal Identification in Mass Disasters*, Stewart, T.D. (ed.). National Museum of Natural History, Washington, D.C., pp. 85–97.

Stern, J.T.J. and Susman, R.L. 1983. The locomotor anatomy of *Australopithecus afarensis*. *American Journal of Physical Anthropology* 60, 279–317.

Swindler, D.R. and Wood, C.D. 1973. *An Atlas of Primate Gross Anatomy*. University of Washington Press, Seattle.

Trinkaus, E. 1983. *The Shanidar Neandertals*. Academic Press, New York.

Trinkaus, E. 1989. Neandertal upper limb morphology and manipulation. In *Hominidae*, Giacobini, G. (ed.). Jaca Book, Turin, pp. 331–338.

Trinkaus, E. and Churchill, S.E. 1988. Neandertal radial tuberosity orientation. *American Journal of Physical Anthropology* 75, 15–21.

Val, A., Dirks, P.H.G.M., Backwell, L. R., d'Errico, F., and Berger, L.R. 2015. Taphonomic analysis of the faunal assemblage associated with the hominins (*Australopithecus sediba*) from the early Pleistocene cave deposits of Malapa, South Africa. *PLoS One* 10, e0126904.

Vallois, H.-V. 1932. L'omoplate humaine. *Bulletin et Mémoires de la Société d'Anthropologie de Paris* 8, 3–153.

Voisin, J.L. 2006. Clavicle, a neglected bone: morphology and relation to arm movements and shoulder architecture in primates. *Anatomical Record* 288, 944–953.

Walker, A.C. and Leakey, R.E. 1993. The postcranial bones. In *The Nariokotome Skeleton*, Walker, A.C. and Leakey, R.E. (eds.). Harvard University Press, Cambridge, pp. 95–160.

Ward, C.V. 2013. Postural and locomotor adaptations of *Australopithecus* species. In *The Paleobiology of* Australopithecus, Reed, K.E., Fleagle, J.G., and Leakey, R.E.F. (eds.). Springer Verlag, Dordrecht, pp. 235–246.

Williams, S.A., Meyer, M.R., Nalla, S., García-Martínez, D., Nalley, T.K., Eyre, J., Prang, T.C., Bastir, M., Schmid, P., Churchill, S.E., and Berger, L.R. 2018 (this volume). The vertebrae, ribs, and sternum of *Australopithecus sediba*. *PaleoAnthropology* 2018, 156–233.

Williams, P.L. and Warwick, R. 1980. *Gray's Anatomy*. W.B. Saunders Company, Philadelphia.

Young, N.M., Capellini, T.D., Roach, N.T., and Alemseged, Z. 2015a. Fossil hominin shoulders support an African ape-like last common ancestor of humans and chimpanzees. *Proceedings of the National Academy of Sciences USA* 112, 11829–11834.

Young, N.M., Capellini, T.D., Roach, N.T., and Alemseged, Z. 2015b. Reply to Melillo: Woranso-Mille is consistent with an australopithecine shoulder intermediate between African apes and *Homo. Proceedings of the National Academy of Sciences of the United States of America* 112, E7160.

Zipfel, B., DeSilva, J.M., Kidd, R.S., Carlson, K.J., Churchill, S.E., and Berger, L.R. 2011. The foot and ankle of *Australopithecus sediba. Science* 333, 1417–1420.